

Tracing Hyperparameter Dependencies for Model Parsing via Learnable Graph Pooling Network

Xiao Guo, Vishal Asnani, Sijia Liu, Xiaoming Liu

Michigan State University

{guoxia11, asnanivi, liusiji5, liuxm}@msu.edu

Abstract. *Model Parsing* defines the research task of predicting hyperparameters of the generative model (GM), given a generated image as input. Since a diverse set of hyperparameters is jointly employed by the generative model, and dependencies often exist among them, it is crucial to learn these hyperparameter dependencies for improved model parsing performance. To explore such important dependencies, we propose a novel model parsing method called Learnable Graph Pooling Network (LGPN). Specifically, we formulate model parsing into a graph node classification task, using graph nodes and edges to represent hyperparameters and their dependencies, respectively. Furthermore, LGPN incorporates a learnable pooling-unpooling mechanism tailored to model parsing, which adaptively learns hyperparameter dependencies of GMs used to generate the input image. We also extend our proposed method to CNN-generated image detection and coordinated attacks detection. Empirically, we achieve state-of-the-art results in model parsing and its extended applications, showing the effectiveness of our method. Our source code will be available upon acceptance.

Keywords: Image Forensics, Forgery Attack Defense, Low-level Vision

1 Introduction

Generative Models (GMs) [12, 20, 31–33, 42, 55], *e.g.*, Generative Adversarial Networks (GANs), Variational Autoencoder (VAEs), and Diffusion Models (DMs), have recently gained significant attentions, offering remarkable capabilities in generating visually compelling images. However, the proliferation of such Artificial Intelligence Generated Content (AIGC) can inadvertently propagate inaccurate or biased information, posing a challenge to information reliability and trustworthiness. To mitigate such the negative impact, various image forensics [50] methods have been proposed, including methods for CNN-generated image detection [7, 19, 22, 51, 57] and manipulation localization [2, 30, 52, 59, 66, 69]. Alongside these defensive efforts, the recent work [3] defines a novel research topic called “*model parsing*”, which predicts GM hyperparameters from generated images (Fig. 1a).

Model parsing is an important research topic, as analyzing GM hyperparameters gains insights into origins of generated images, enabling defenders to develop

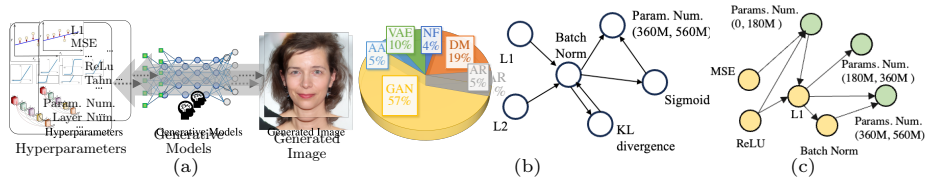


Fig. 1: (a) Hyperparameters define a GM that generates images. *Model parsing* [3] refers to the task of predicting hyperparameters given the generated image (Sec. 3.1) (b) We study the co-occurrence pattern among different hyperparameters in different GMs from the RED140 dataset, and subsequently construct a directed graph to capture dependencies among these hyperparameters (Sec. 3.1). RED140’s composition is shown as the pie chart¹. (c) We define the discrete-value graph node (■) (e.g., L1 and Batch Norm) for each discrete hyperparameter. For each continuous hyperparameter (■), we partition its range into n distinct intervals, and each interval is then represented by a graph node: **Parameter Number** has three corresponding continuous-value graph nodes. Representations on these graph nodes are used to predict hyperparameters (Sec. 3.4).

effective countermeasures against falsified content. Specifically, it is discovered in the previous work [3] that 37 hyperparameters can be predicted using the generated image as input (details in Sec. 3.1). However, their approach primarily focuses on finding correlations among GMs using a clustering-based method, neglecting the learning of dependencies among these 37 hyperparameters. To address this limitation, we formulate model parsing into a graph node classification problem and then propose a framework to capture hyperparameter dependencies, leveraging the effectiveness of Graph Convolution Network (GCN) in capturing the correlation among graph nodes [17, 34, 49, 56].

More formally, we first use training samples in the RED dataset to construct a direct graph (Fig. 1b). The directed graph, based on the label co-occurrence pattern, illustrates the fundamental correlation between different categories and helps prior GCN-based methods achieve remarkable performances in various applications [8, 11, 16, 45, 53, 62]. In this work, this directed graph is tailored to the model parsing — we define discrete-value and continuous-value graph nodes to represent hyperparameters (Fig. 1c). Then, we use this graph to formulate model parsing into a graph node classification problem, in which the discrete-value graph node feature decides if a given hyperparameter is used in the given GM, and the continuous-value node feature decides which range the hyperparameter resides. This formulation helps obtain effective hyperparameters representation and dependencies among them for the model parsing task (Sec. 3.1).

To this end, we propose a novel model parsing framework called Learnable Graph Pooling Network (LGPN). LGPN contains a dual-branch feature extractor and a GCN refinement block (Fig. 2). Our dual-branch feature extractor differs from neural network backbones used in current high generalization ability detection methods [5, 57, 58, 58, 67], using down-sampling operations (e.g.,

¹ We adhere to the naming of the previous work [3], as the pie chart of Fig. 1b, in which AA, AR and NF represent Adversarial Attack models, Auto-Regressive models and Normalizing Flow models, respectively.

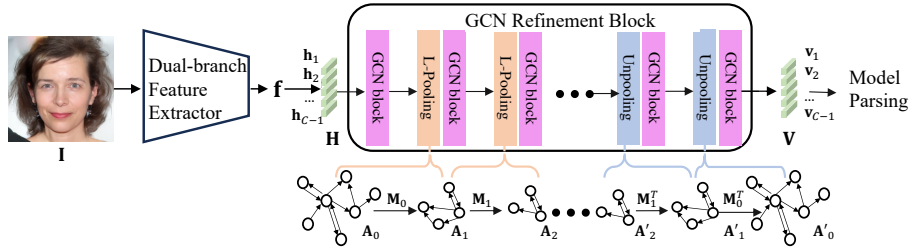


Fig. 2: Learnable Graph Pooling Network. Given an input image I , the proposed LGPN first uses the dual-branch feature extractor (Fig. 3) to extract the representation \mathbf{f} . The learned representation \mathbf{f} contains information about the generation trace, so it can help different image forensics tasks. Then, \mathbf{f} is transformed into \mathbf{H} , which represents a set of graph node features and is fed into the GCN refinement block. The GCN refinement block stacks GCN layers with paired pooling-unpooling layers (Sec. 3.2) and produces the refined feature \mathbf{V} for model parsing. Our method is jointly trained with 3 different objective functions (Sec. 3.3).

pooling) gradually reduce the learned feature map resolution during the forward propagation. This down-sampling can cause the loss of already subtle generation traces left by GMs. Instead, our dual-branch feature extractor leverages a high-resolution representation that largely preserves the information of generation traces throughout the forward propagation (Sec. 3.2). Therefore, the learned image representation from the dual-branch feature extractor deduces the crucial information of used GMs and benefits model parsing. Subsequently, this representation is transformed into a set of graph node features, along with the pre-defined directed graph, which are fed to the GCN refinement block. The GCN refinement block contains trainable pooling layers that progressively convert the correlation graph into a series of coarsened graphs, by merging original graph nodes into supernodes. Then, the graph convolution is conducted to aggregate node features at all levels of graphs, and trainable unpooling layers are employed to restore supernodes to their corresponding children nodes. This learnable pooling-unpooling mechanism helps LGPN generalize to parsing hyperparameters in unseen GMs and improves the GCN representation learning.

In addition to model parsing, we apply the proposed LGPN on the *coordinated attacks detection* [3], assessing its effectiveness in identifying whether two fake images originate from the same GM. Furthermore, we extend the dual-branch feature extractor to *CNN-generated image detection* and *image attribution*, aiming to demonstrate its superiority in detecting generation traces. Sec. 3.4 details these three applications. In summary, our contributions are:

- ◊ We design a novel way to formulate the *model parsing* as a graph node classification task, using a directed graph to help capture hyperparameter dependencies for the better model parsing performance.

- ◊ A learnable pooling-unpooling mechanism is introduced with GCN to enhance representation learning in model parsing and its generalization ability.

- ◊ We introduce a simple yet effective dual-branch feature extractor that leverages the high-resolution representation to better preserve generation traces dur-

ing the forward propagation. This approach benefits different image forensic tasks, including model parsing and CNN-generated image detection.

◊ We evaluate our method on four image forensic applications: model parsing, CNN-generated image detection, coordinated attacks detection, and image attribution. The promising results of these evaluations showcase the effectiveness of our approach in learning and identifying generation traces.

2 Related Works

Model Parsing Unlike previous model parsing works [4, 29, 46, 54] that require prior knowledge of machine learning models and their inputs to predict training information or model hyperparameters, Asnani *et al.* [3] recently proposes a technique to estimate 37 pre-defined hyperparameters based on generated images. This work [3] uses a fingerprint estimation network that is trained with four constraints to estimate the fingerprint for each image. After that, a parsing network is employed to use such distinctive fingerprints for estimating hyperparameters. However, they overlook the dependencies among hyperparameters, which cannot be adequately captured by the estimated mean and standard deviation. In contrast, we propose LGPN, using GCN to model the dependency between different hyperparameters, improving the overall model parsing performance.

GCN-based Method Graph Convolution Neural Network (GCN) show effectiveness in encoding dependencies among different graph nodes [17, 25, 27, 34, 56], and in the computer vision community, directed graphs based on label co-occurrence patterns are used with GCN in tasks such as multi-label image recognition [8, 11, 62], semantic segmentation [10, 16, 28, 38], and person ReID and temporal action localization [9, 45, 53, 60]. These works utilize GCNs to learn dependencies among various entities by reweighting the correlation matrix through techniques such as attention and gate mechanisms. However, our approach diverges from this by using the pooling algorithm to alter the graph structure, enhancing GCN’s representation learning. Also, Graph U-Net [18] shares similarities with our GCN refinement block, whereas their pool operation forms a smaller graph by removing some unimportant nodes. This approach may not be suitable for model parsing, where each node feature represents the corresponding hyperparameter and needs to be preserved.

Learning Image Generation Traces All GMs leave particular traces in their generated images [13, 41], which can be visualized through spatial artifacts or evident peaks in the frequency domain [57, 67]. These traces serve as important clues for image forensic tasks such as detection [13, 57, 67], attribution [22, 64] and model parsing [3, 61]. Current methods [5, 57, 58, 58, 67] use backbones like ResNet and XceptionNet, known for their high generalization abilities. However, these models often employ downsampling operations, like convolutions with large strides and pooling, which help capture global semantics yet discard high-frequency information containing generation traces. By contrast, we propose a simple yet effective dual-branch feature extractor that leverages a special high-resolution representation for capturing such generation traces, and its effectiveness is evaluated in the comparison to recent detection methods [47, 58].

3 Method

In this section, we first revisit some fundamental preliminaries in Sec. 3.1, and Sec. 3.2 introduces the proposed Learnable Graph Pooling Network (LGPN). Lastly, we describe the training (Sec. 3.3) and inference procedures with extended applications (Sec. 3.4) of our method.

3.1 Preliminaries

This section reports the problem statement of *model parsing* and its formulation as a graph node classification task with Graph Convolutional Networks (GCN).

Revisiting Model Parsing Given the input image $\mathbf{I} \in \mathbb{R}^{3 \times W \times H}$ generated via GM (*i.e.*, \mathcal{G}), the algorithm generates three vectors ($\mathbf{y}^d \in \mathbb{R}^{18}$, $\mathbf{y}^c \in \mathbb{R}^9$ and $\mathbf{y}^l \in \mathbb{R}^{10}$) as the prediction of C hyperparameters used in the \mathcal{G} . Specifically, defined by work [3], these predictable C hyperparameters include discrete and continuous architecture hyperparameters, as well as loss functions, which are denoted as \mathbf{y}^d , \mathbf{y}^c , and \mathbf{y}^l , respectively. For discrete architecture hyperparameters (\mathbf{y}^d) and loss functions (\mathbf{y}^l) vectors, each element is a binary value representing if the corresponding feature is used or not. For the continuous architecture hyperparameters vector (\mathbf{y}^c), each element is the value of certain continuous architecture hyperparameters, such as layer number and parameter number. As these hyperparameters are in different ranges, we normalize them into $[0, 1]$, same as [3]. Predicting \mathbf{y}^d and \mathbf{y}^l is a classification task while the regression is used for \mathbf{y}^c . The detailed definition is in Tab. 1 and 2 of the supplementary.

The previous work collected 116 different GMs (termed as RED116) to study model parsing. We augment RED116 with different diffusion models such as DDPM [26], ADM [15] and Stable Diffusions [48], to increase the spectrum of GMs. Secondly, to make the trained model learn the generation artifacts, we have added real images, on which these GMs are trained, into the dataset. In the end, we have collected 140 GMs in total. We denote this dataset as RED140. More details are in the supplementary Sec. 4.

Correlation Graph Construction We design a graph structure of model parsing, where graph nodes and edges represent hyperparameters and their dependencies, respectively. We first use conditional probability $P(L_j|L_i)$ to denote the probability of hyperparameter L_j occurrence when hyperparameter L_i appears. We count the occurrence of such pairs in the RED140 to retrieve the matrix $\mathbf{G} \in \mathbb{R}^{C \times C}$ (C is the number of hyperparameter), and \mathbf{G}_{ij} denotes the conditional probability of $P(L_j|L_i)$. Then, we apply a fixed threshold τ to eliminate edges with low correlations. Therefore, we obtain a directed graph $\mathbf{A} \in \mathbb{R}^{C \times C}$, where \mathbf{A}_{ij} indicates if there exists an edge between node i and j .

Specifically, as depicted in Fig. 1c, each discrete hyperparameters (*e.g.*, discrete architecture hyperparameters and loss functions) is represented by one graph node, denoted as discrete-value graph node. For continuous hyperparameters, we first divide the range into n different intervals, and each of intervals is represented by one graph node, termed as continuous-value graph node. Subsequently, we use discrete-value graph nodes to decide if given hyperparameters are

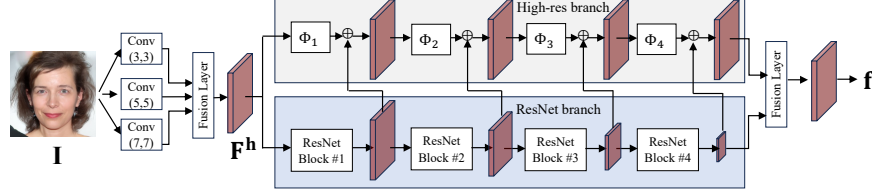


Fig. 3: The dual-branch feature extractor. First, convolution layers with different kernel sizes extract feature maps of the input image \mathbf{I} . A fusion layer concatenates these feature maps and then proceeds the concatenated feature to the ResNet branch and High-res branch. ResNet branch consists of pre-trained ResNet blocks, while the high-res branch maintains the high-resolution representation to help detect generation traces. Lastly, output features of two branches are combined, denoted as \mathbf{f} , which can be directly used for CNN-generated image detection and image attribution (Sec. 3.4).

present, and the continuous-value node decides which range the hyperparameter resides.

Stack Graph Convolution Layers Given the directed graph \mathbf{A} , we denote the stacked graph convolution operation as:

$$\mathbf{h}_i^l = \text{ReLU}\left(\sum_{j=1}^N \mathbf{A}_{i,j} \mathbf{W}^l \mathbf{h}_j^{l-1} + \mathbf{b}^l\right), \quad (1)$$

where \mathbf{h}_i^l represents the i -th node feature in graph \mathbf{A} , and \mathbf{W}^l and \mathbf{b}^l are corresponding weight and bias terms. Empirically, different nodes in the graph have different degrees, resulting in drastically different magnitudes for aggregated node features. This can impair the node representation because learning is always biased towards high-degree nodes. Therefore, we formulate Eq. 1 into:

$$\mathbf{h}_i^l = \text{ReLU}\left(\sum_{j=1}^N \hat{\mathbf{A}}_{i,j} \mathbf{W}^l \mathbf{h}_j^{l-1} / d_i + \mathbf{b}^l\right), \quad (2)$$

where $\hat{\mathbf{A}} = \mathbf{A} + \mathbf{I}$ and \mathbf{I} is an $n \times n$ identity matrix, and d_i is degree of node i , namely, $d_i = \sum_{j=1}^n \hat{\mathbf{A}}_{ij}$.

3.2 Learnable Graph Pooling Network

In this section, we detail the dual-branch feature extractor and GCN refinement block—two major components used in the proposed LGPN, as depicted in Fig. 2.

Dual-branch Feature Extractor As shown in Fig. 3, the dual-branch feature extractor uses one branch (*i.e.*, ResNet branch) to propagate the original image information. Meanwhile, the other branch, denoted as *high-res branch*, harnesses the high-resolution representation that helps detect high-frequency generation artifacts stemming from various GMs. More formally, three separate 2D convolution layers with different kernel sizes (*e.g.*, 3×3 , 5×5 and 7×7) are utilized to extract feature maps of given the image \mathbf{I} . We concatenate these feature maps and feed them to the fusion layer—the 1×1 convolution kernel for the channel

dimension reduction. Then, we obtain the feature map $\mathbf{F}^h \in \mathbb{R}^{D \times W \times H}$, with the same resolution as \mathbf{I} . After that, we proceed \mathbf{F}^h to the dual-branch backbone. Specifically, the ResNet branch, with four pre-trained blocks, exhibits high generalization ability in detecting unseen GMs [47, 57]. We upsample intermediate features output from each ResNet block and incorporate them into the high-res branch, as depicted in Fig. 3. The high-res branch also has four different convolution blocks (*e.g.*, Φ_b with $b \in \{1 \dots 4\}$), which do not employ down-sampling operations, such as the 2D convolution with large strides and pooling layers. Therefore, intermediate feature maps throughout the high-res branch possess the same resolution as \mathbf{F}^h .

In the end, ResNet branch and high-res branch output feature maps are concatenated for the richer representation and then pass through an AVGPOOL. The final learned representation, $\mathbf{f} \in \mathbb{R}^D$, learns to capture generation artifacts of the given input image \mathbf{I} . We learn C independent linear layers, *i.e.*, $\Theta = \{\theta_{i=0}^{C-1}\}$ to transform \mathbf{f} into a set of graph node features $\mathbf{H} = \{\mathbf{h}_0, \mathbf{h}_1, \dots, \mathbf{h}_{(C-1)}\}$, where $\mathbf{H} \in \mathbb{R}^{C \times D}$ and $\mathbf{h}_i \in \mathbb{R}^{1 \times D}$ ($i \in \{0, 1, \dots, C-1\}$). We use \mathbf{H} to denote graph node features of the directed graph (*i.e.*, graph topology) $\mathbf{A} \in \mathbb{R}^{C \times C}$.

GCN Refinement Block The GCN refinement block has a learnable pooling-unpooling mechanism which progressively coarsens the original graph \mathbf{A}_0 into a series of coarsened graphs $\mathbf{A}_1, \mathbf{A}_2 \dots \mathbf{A}_n$, and graph convolution is conducted on graphs at all different levels. Specifically, such a pooling operation is achieved by merging graph nodes, namely, via a learned matching matrix \mathbf{M} . Also, the correlation matrices of different graphs, denoted as \mathbf{A}_l ², are learned using MLP layers, which are also influenced by the GM responsible for generating the input image. This further emphasizes the significant impact of GM on the correlation graph generation process.

Learnable Graph Pooling Layer First, $\mathbf{A}_l \in \mathbb{R}^{m \times m}$ and $\mathbf{A}_{l+1} \in \mathbb{R}^{n \times n}$ denote directed graphs at l th and $l+1$ th layers, with m and n ($m \geq n$) graph nodes, respectively. An assignment matrix $\mathbf{M}_l \in \mathbb{R}^{m \times n}$ to convert \mathbf{A}_l to \mathbf{A}_{l+1} as:

$$\mathbf{A}_{l+1} = \mathbf{M}_l^T \mathbf{A}_l \mathbf{M}_l. \quad (3)$$

Also, we use $\mathbf{H}_l \in \mathbb{R}^{m \times D}$ and $\mathbf{H}_{l+1} \in \mathbb{R}^{n \times D}$ to denote graph node features of \mathbf{A}_l and \mathbf{A}_{l+1} , where each graph node feature is D dimensional. Therefore, we can use \mathbf{M}_l to perform the graph node aggregation via:

$$\mathbf{H}_{l+1} = \mathbf{M}_l^T \mathbf{H}_l. \quad (4)$$

For simplicity, we use f_{GCN} to denote the mapping function that is imposed by a GCN block which has multiple GCN layers. \mathbf{H}_l^{in} and \mathbf{H}_l^{out} are the input and output feature of the l th GCN blocks:

$$\mathbf{H}_l^{out} = f_{GCN}(\mathbf{H}_l^{in}). \quad (5)$$

Ideally, the pooling operation and correlation between different hyperparameters should be dependent on the extracted feature of the given input image, \mathbf{f} .

² A graph at l -th layer and its correlation can be denoted as \mathbf{A}_l .

Therefore, assuming the learned feature at l th layer is \mathbf{H}_l^{out} , we use two separate weights \mathbf{W}_m and \mathbf{W}_a to learn the matching matrix \mathbf{M}_l and adjacency matrix \mathbf{A}_l at l th layer as:

$$\mathbf{M}_{l+1} = \text{softmax}(\mathbf{W}_m \mathbf{H}_l^{out}); \mathbf{A}_{l+1} = \frac{1}{1 + e^{-\alpha(\mathbf{W}_a \mathbf{H}_l^{out})}}, \quad (6)$$

where α is set as $1e9$. As a result, we obtain the assignment matrix with values exclusively set to 0 or 1. After several levels of graph pooling, LGPN encodes information with an enlarged receptive field into the coarsened graph.

Learnable Unpooling Layer We perform the graph unpooling operation, which restores the information to the graph at the original resolution for the original graph node classification task. As Fig. 2, to avoid confusion, we use \mathbf{H} and \mathbf{V} to represent the graph node feature on the pooling and unpooling branch, respectively. The correlation matrix on the unpooling branch is denoted by \mathbf{A}' ,

$$\mathbf{A}'_{l-1} = \mathbf{M}_l \mathbf{A}'_l \mathbf{M}_l^T; \mathbf{V}_{l-1} = \mathbf{M}_l \mathbf{V}_l, \quad (7)$$

where \mathbf{A}'_l and \mathbf{A}'_{l-1} are the l th and $l-1$ th layers in the unpooling branch. Finally, we use the refined feature \mathbf{V} for the model parsing, as depicted in Fig. 2.

Discussion This learnable pooling-unpooling mechanism offers three distinct advantages. Firstly, each supernode in the coarsened graph serves as the combination of features from its children nodes, and graph convolutions on supernodes have a large receptive field for aggregating features. Secondly, the learnable correlation adapts and models hyperparameter dependencies dynamically based on generation artifacts of input image features (*e.g.*, \mathbf{f}). Lastly, learned correlation graphs \mathbf{A} vary across different levels, which can also address the issue of over-smoothing commonly encountered in GCN learning [6, 37, 43].

3.3 Training Objectives

We jointly train our method with three objective functions. Graph node classification loss (*e.g.*, \mathcal{L}^{graph}) encourages each graph node feature to predict the corresponding hyperparameter label. Artifacts isolation loss (*e.g.*, \mathcal{L}^{iso}) helps the LGPN only parse the hyperparameters for generated images, and hyperparameter hierarchy constraints (*e.g.*, $\mathcal{L}^{hier.}$) imposes hierarchical constraints among different hyperparameters while stabilizing the training.

Training Samples We denote a training sample as $\{\mathbf{I}, \mathbf{y}\}$, where \mathbf{I} is the input image and $\mathbf{y} = \{y_0, y_1, \dots, y_{(C-1)}\}$ is its annotation for C parsed hyperparameters as introduced in Sec. 3.1. Specifically, y_c is assigned as 1 if the sample has c -th hyperparameter and 0 otherwise, where $c \in \{0, 1, \dots, C-1\}$. Details are in Supplementary Sec. 2.

Graph Node Classification Loss Given image \mathbf{I} , we convert the refined feature \mathbf{V} into the predicted score vector, denoted as $\mathbf{s} = \{s_0, s_1, \dots, s_{(C-1)}\}$. We employ the sigmoid activation to retrieve the corresponding probability vector $\mathbf{p} = \{p_0, p_1, \dots, p_{(C-1)}\}$, namely, $p_c = \text{SIGMOID}(s_c)$. Then, we have:

$$\mathcal{L}^{graph} = \sum_{c=0}^{C-1} (y_c \log p_c + (1 - y_c) \log(1 - p_c)). \quad (8)$$

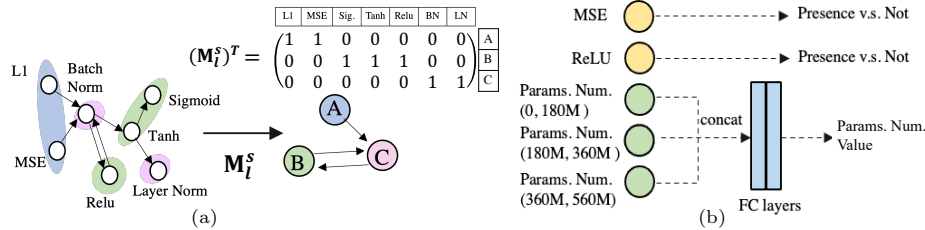


Fig. 4: (a) The toy example of the hyperparameter hierarchy assignment \mathbf{M}_l^s : both L1 and L2 belong to the category of pixel-level loss function, such that they are merged into the supernode A. Nonlinearity functions (*e.g.*, ReLU and Tanh) and normalization methods (*e.g.*, Layer Norm. and Batch Norm.) are merged into supernodes B and C, respectively. (b) In the inference, discrete-value graph node features are used to classify if discrete hyperparameters are used in the given GM. We concatenate corresponding continuous-value graph node features and regress the continuous hyperparameter value.

Hyperparameter Hierarchy Prediction Fig. 4 shows that different hyperparameters can be grouped, so we define the hyperparameter hierarchy assignment \mathbf{M}^s to reflect this inherent nature. More details of such the assignment are in supplementary Sec. 1. Suppose, at the layer l th, we minimize the L_2 norm of the difference between the predicted matching matrix \mathbf{M}_l and \mathbf{M}_l^s ,

$$\mathcal{L}^{hier} = \|\mathbf{M}_l^s - \mathbf{M}_l\|_2 = \sqrt{\sum_{i,j=0} (m_{ij}^s - m_{ij})^2}. \quad (9)$$

Artifacts Isolation Loss We denote the image-level binary label as y^{img} and use p^{img} as the probability that \mathbf{I} is a generated image. Then we have:

$$\mathcal{L}^{iso} = \sum_{i=0}^{M-1} (y^{img} \log p^{img} + (1 - y^{img}) \log(1 - p^{img})). \quad (10)$$

In summary, our joint training loss function can be written as $\mathcal{L}^{all} = \lambda_1 \mathcal{L}^{graph} + \lambda_2 \mathcal{L}^{hier} + \lambda_3 \mathcal{L}^{iso}$, where λ_1 and λ_2 equal 0 when \mathbf{I} is real.

3.4 Inference and Applications

We apply the trained model on model parsing and extend the proposed dual-branch feature extractor to tasks like CNN generated image detection and image attribution.

Model Parsing As Fig. 4b, we use the discrete-value graph node feature to perform the binary classification to decide the presence of given hyperparameters. For the continuous architecture hyperparameter, we first concatenate n corresponding node feature and train a linear layer to regress it to the estimated value. Empirically, we set n as 3 and show this concatenated feature improves the robustness in predicting the continuous value. (see the supplementary Sec. 3).

CNN-generated Image Detection. We obtain a binary detector by replacing the GCN refinement module with a shallow network that takes learned features

	Method			Loss Function		Dis. Archi. Para.		Con. Archi. Para.
	ID	Backbone	MP Head	F1 ↑	Acc. ↑	F1 ↑	Acc. ↑	L1 error ↓
1	Baseline1	ResNet-50	MLP	0.790	0.777	0.721	0.690	0.163
2	Baseline2	HR-Net	MLP	0.807	0.819	0.722	0.703	0.149
3	Baseline3	ViT-B	MLP	0.763	0.759	0.683	0.664	0.177
4	Baseline4	Dual-branch	MLP	0.825	0.809	0.757	0.709	0.135
5	FEN-PN [3]	FEN.	Parsing Net.	0.805	0.789	0.730	0.708	0.139
6	LGPN	Dual-branch	GCN refinement	0.846	0.833	0.795	0.775	0.120

Table 1: We report model parsing performance on RED140, where each method has an individual ID that represents different backbones and model parsing (MP) heads. *Loss Function* reports the averaged prediction performance on 10 loss functions. The averaged performance on 18 discrete architecture hyperparameters and 9 continuous hyperparameters are reported in *Dis. Archi. Para.* and *Con. Archi. Para.*, respectively. [**Bold:** best result].

f from the dual-branch feature extractor and outputs binary detection results, distinguishing generated images from real ones. Results are reported in Sec. 4.2.

Coordinated Attacks Detection . Coordinate attacks detection [3] classify if two given images are generated from the same or different models. Coordinated attacks pose a challenge for existing image forensic approaches such as image attribution [22, 64] and CNN-generated image detection [57], which may struggle with performance when confronted with fake images generated by unseen GMs. In contrast, model parsing, which leverages predicted hyperparameter representation as descriptors for GMs, can effectively solve this task. Specifically, we first denote the input image pair as $(\mathbf{I}_1, \mathbf{I}_2)$, and we apply LGPN to obtain the refined feature $(\mathbf{V}_1, \mathbf{V}_2)$. We train a shallow network on $(\mathbf{V}_1, \mathbf{V}_2)$ to predict if $(\mathbf{I}_1, \mathbf{I}_2)$ are generated by the same GM. Details are in Sec. 4.3.

Image Attribution Similar to CNN-generated image detection, we use a shallow network to replace the GCN refinement block for the image attribution task, which defines a multi-class task, depending on the number of GMs used during the training. Details are reported in Sec. 4.4.

4 Experiment

4.1 Model Parsing

RED140 has 140,000 images in total, in which each GM contains 1,000 images with various semantics including objects, handwritten digits, and human faces. We follow the protocol of [3]: we divide samples into 4 disjoint sets and conduct 4-fold cross-validation. Each partition comprises different GM categories (*e.g.*, GAN, VAE, etc). We train our model on the 104 GMs from three sets to predict 37 hyperparameters. The evaluation is conducted on GMs in one remaining test set. The performance is averaged across four sets, measured by F1 score and AUC for discrete hyperparameters (loss function and discrete architecture hyperparameters) and L1 error for continuous architecture hyperparameters. Details are in supplementary Sec. 3.

Main Performance We report the model parsing performance in Tab. 1, where our proposed LGPN (line #6) largely outperforms the previous model parsing

Method		Loss Function		Dis. Archi. Para.		Training Objectives			Performance	
Backbone	MP Head	F1 \uparrow	Acc. \uparrow	F1 \uparrow	Acc. \uparrow	L_{graph}	L_{iso}	L_{hier}	Loss Fun.	Dis. Archi. Para.
1	MLP	0.825	0.809	0.757	0.709	1	✓		0.837	0.770
2	Stacked GCN	0.832	0.813	0.769	0.738	3	✓	✓	0.840	0.781
3	Att-GCN [56]	0.834	0.827	0.780	0.745	2	✓	✓	0.839	0.790
4	Graph U-Net [18]	0.822	0.820	0.748	0.702	4	✓	✓	0.846	0.795
5	GCN refinement	0.846	0.833	0.795	0.775					

(a) The model with different GCN variants.

(b) The ablation study on training objectives (F1).

Table 2: (a) We compare different GCN variants for the model parsing performance; (b) the ablation on our three objective functions, defined in Sec. 3.3.

algorithms. We first employ commonly used backbones to set up competitive model parsing baselines for a more comprehensive comparison. Specifically, four baselines in lines #1—4 that use ViT-B, ResNet-50, HR-Net and dual-branch feature extractor as backbones with 2 layers MLP as the model parsing head, respectively. Baseline4 (line #4) achieve the best performance, which indicates that the dual-branch feature extractor is the most suitable backbone for model parsing, because Baseline4 has 1.8% and 3.5% higher F1 score over the Baseline2 that uses HR-Net on predicting hyperparameters of loss functions and discrete architecture. After that, we report the performance of the previous work FEN-PN, which already proves its effectiveness on the model parsing task, because it has specific model parsing architectures containing a fingerprint estimate network (FEN) and a parsing network that predicts hyperparameters. Surprisingly, it only achieves comparable performance as Baseline2. We hypothesize that the performance drop is because FEN-PN is less effective in predicting hyperparameters of diffusion models, and RED140 dataset has more images from diffusion models than RED116 on which FEN-PN achieves competitive results. We report the complete performance comparison on RED116 in the supplementary Tab. 5. Lastly, we replace MLP with the GCN refinement block, which is the full model of LGPN (line #6). The full LGPN performs better on all metrics, indicating that the proposed GCN refinement block indeed refines the graph node feature and makes an effective model parsing head than MLP layers.

Ablation Study Tab. 2 reports the ablation study. First, Tab. 2a shows we use different GCN variants as the model parsing head. By comparing lines #1 and #2, we conclude that replacing MLP layers with the GCN benefits the model parsing task. After all, GCN leverages the structural information of the pre-defined graph, helping capture the dependencies among different hyperparameters. Then, we use *Graph attention networks* [56] (Att-GCN) at line #3, which employs the attention mechanism to update the graph node feature. As a result, Att-GCN achieves 1.1% higher F1 than stacked GCN (*e.g.*, line #2) on predicting discrete architecture parameters. Lastly, line #4 uses *Graph U-Net* [18], which has a similar pooling-unpooling mechanism to our GCN refinement block, but its pooling operation is discarding graph nodes in the previous layer for forming a smaller graph. Using the Graph U-Net as the model parsing head produces the worse predicting performance on discrete architecture hyperparameters — 4.3% lower accuracy than Att-GCN (#3). We believe this is because dropping graph nodes is not optimal for model parsing, in which all graph nodes repre-

sent the corresponding hyperparameters and are important for the final parsing performance. By contrast, LGPN merges the children nodes into the supernode, such that all node information in the previous layer remains in the smaller pooled graph. Our proposed pooling-unpooling mechanism’s superiority is supported by the fact that Line #5 achieves the best model parsing performance in the Tab. 2a.

Tab. 2b shows the ablation analysis on different training objective functions we use. Line #1 only optimizes the LGPN with \mathcal{L}^{grpah} , producing results comparable to simply stacking GCN with the attention mechanism (e.g., line #3 in Tab. 2a). Line #2 and #3 shows the performance brought from \mathcal{L}^{iso} and \mathcal{L}^{hier} , which improve the performance by 1.1% and 2.0% than only using \mathcal{L}^{grpah} , on predicting discrete architecture hyperparameters, respectively. This is because \mathcal{L}^{iso} and \mathcal{L}^{hier} help the LGPN concentrate learning generation traces from generated images and impose the hierarchical constraints, respectively. With all three critical training objective functions, LGPN achieves a more competitive performance.

Analysis Fig. 1 and 6 in the supplementary reports the detailed performance of each hyperparameter and GM. Such results can further demonstrate that GCN, capturing hyperparameters dependencies, helps the model parsing task. For example, in Fig. 1c, LGPN shows L1 errors of 0.147 and **0.081** on Layers Num. and Param. Num. respectively, whereas the model without GCN only achieves 0.149 and 0.148, respectively. This is because of the dependency between Param. Num. and Layer Num. help decrease the L1 error on Param. Num. prediction. This dependency aligns with the observation that models with more Layers Num. can have more Param. Num.. Secondly, Fig. 5 shows that learned correlation graphs (\mathbf{A}'_0) from image pairs exhibit significant similarity when both images belong to the same *unseen* GM. This result demonstrates that our correlation graph largely depends on the GM instead of image content, given that we have different contents (e.g., human face and objects) in unseen GMs from each test.

4.2 CNN-generated Image Detection

For CNN-generated image detection, we first obtain the binary detector introduced in Sec. 3.4. Then, we follow the experiment setup from prior works [47, 57, 68], which trains the model on images generated by ProGAN [31], and tests

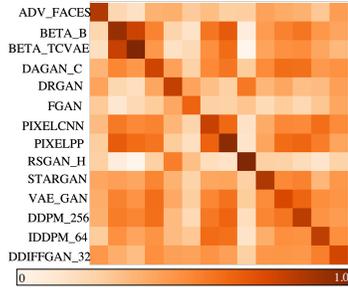


Fig. 5: Cosine similarity between generated correlation graphs (i.e., \mathbf{A}'_0) for *unseen* GMs in one of four test sets. Each element of this matrix is the average cosine similarities of 2,000 pairs of generated correlation graphs \mathbf{A}'_0 from corresponding GMs. The diagonal of this matrix shows two images from the same GM have highly similar correlation graphs. Matrices for the other three test sets are in Fig. 3 of the supplementary.

Detection method	Variant	Generative Adversarial Networks						Deepfakes		Low level vision		Perceptual loss		Average
		Pro-GAN	Cycle-GAN	Big-GAN	Style-GAN	Gau-GAN	Star-GAN	FF++	SITD	SAN	CRN	IMLE		
Trained network [57]	Blur+JPEG (0.1)	100.0	93.47	84.50	99.54	89.49	98.15	89.02	73.75	59.47	98.24	98.40	89.45	
	Blur+JPEG (0.5)	100.0	96.83	88.24	98.29	98.09	95.44	66.27	86.0	61.2	98.94	99.52	89.89	
	ViT:CLIP (0.5)	99.98	93.32	83.63	88.14	92.81	84.62	67.23	93.48	55.21	88.75	96.22	85.77	
Patch classifier [5]	ResNet50-Layer1	98.86	72.04	68.79	92.96	55.9	92.06	60.18	65.82	52.87	68.74	67.59	72.34	
	Xception-Block2	80.88	72.84	71.66	85.75	65.99	69.25	76.55	76.19	76.34	74.52	68.52	74.41	
Co-occurrence [44]	-	99.74	80.95	50.61	98.63	53.11	67.99	59.14	68.98	60.42	73.06	87.21	72.72	
Freq-spec [68]	CycleGAN	55.39	100.0	75.08	55.11	66.08	100.0	45.18	47.46	57.12	53.61	50.98	64.18	
Universal detector [47]	NN, $k = 1$	100.0	98.14	94.49	86.68	99.26	99.53	93.09	78.46	67.54	83.13	91.07	90.12	
	LC	100.0	99.46	99.59	97.24	99.98	99.60	82.45	61.32	79.02	96.72	99.00	92.21	
Ours		100.0	97.03	97.76	99.96	98.97	99.65	93.50	98.42	85.00	99.60	99.90	97.27	

Table 3: CNN-generated image detection performance measured by Average Precision on 11 forgery methods containing face and non-face images. Previous methods’ quantitative results are taken from [47]. [**Bold:** best result; **Blue:** second best result].

on images generated by other unseen GMs. Specifically, Tab. 3 shows the performance on 11 forgery methods benchmarked by the previous work, and Tab. 4 shows the performance on images from diffusion models and the commercial software³. Same measurements as the previous work, we use the average precision (AP) in Tab. 3 and 4 and accuracy in supplementary’s Tab. 7 and 8. Tab. 3 shows our proposed dual-branch feature can achieve premium detection performance compared to prior methods. Specifically, the average AP is 5.06% higher than the second-best result, which leverages pre-trained CLIP features for the high generalization ability in detecting images from unseen GMs. We believe such a performance advantage comes from the high-resolution branch in the dual-branch feature extractor, maintaining the high-resolution representation that effectively exploits subtle generation traces left from generation procedures.

Moreover, Tab. 4 reports the detection performance on a more challenging scenario. This is because we only use ProGAN as the training data, yet test images are generated from diffusion models and Celeb-DF [39] that employ various data post-processing steps to reduce the artifact. Nevertheless, our proposed method still surpasses the ResNet50 baseline by a large margin in detecting images generated from DALL-E2 and Midjourney that have compelling visual content. This performance improvement demonstrates the robustness of the high-resolution representation employed in our method, in terms of detecting images from inter-domain generation methods.

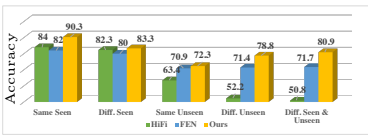
Detection method	Deep fakes		Diffusion models			Commercial			Average
	Celeb-DF	DD-PM	DD-IM	GLIDE	LDM	DALL-E2	Mid Jour.	SORA	
ResNet (0.1) [57]	89.0	72.33	70.11	69.4	80.55	72.4	57.50	52.51	70.47
ResNet (0.5) [57]	84.5	71.04	67.54	71.3	75.20	74.1	64.30	57.32	70.63
Universal detector [47]	66.28	91.43	91.47	92.98	92.81	98.91	60.93	66.52	82.66
DIRE [58]	78.78	85.31	80.37	86.38	88.71	74.53	51.50	54.51	75.01
Ours	91.11	90.59	88.00	93.19	93.91	95.17	70.00	67.72	86.69

Table 4: CNN-generated image detection performance by average precision on images generated via deepfakes (*e.g.*, Celeb-DF [40]), diffusion models (10k images for each category), and commercial softwares. [**Bold:** best result].

³ The released benchmark of the work [47] only contains 1k images for each diffusion model, which are insufficient for the convincing evaluation. Therefore, we produce Tab. 4 with more test images from diffusion models and detailed performance on a released benchmark of work [47] in the supplementary

Method	Acc.	AUC	Pd@5%
HiFi. [22]	72.3	75.4	30.4
FEN-PN. [3]	83.0	92.4	61.2
LGPN <i>w/o</i> GCN	83.9	92.2	62.5
LGPN <i>w/o</i> pooling	84.6	94.2	68.6
LGPN*	85.9	95.7	72.3

(a)



Method	CelebA	LSUN
PRNU [41]	86.61	67.84
Attr. [65]	99.43	98.58
FEN-PN [3]	99.66	99.84
Ours	99.79	99.73

(c)

Table 5: (a) The average coordinate attack detection performance on 4-fold cross validation. (b). Test image pairs in coordinate attack detection are from one of 5 cases, bar charts from left to right: same and different GMs in seen set; same or different GMs in unseen set; one GM is from seen set and the other from unseen set. (c) Image attribution performance is measured by the classification accuracy.

4.3 Coordinate Attack Detection

As detailed in Sec. 3.4, we evaluate coordinated attack detection on RED140 in a 4-fold cross-validation. In each fold, the train set has 125 GMs, and the test set has 30 GMs where 15 GMs are exclusive (unseen) from the train set and 15 GMs are seen in the train set. We use the average of the 4 folds as final results. For the measurement, we use accuracy, AUC and probability of detection at a fixed false alarm rate (Pd@FAR) *e.g.*, Pd@5%. These metrics are commonly used in biometric applications [1, 21, 24]. Specifically, we compare against FEN-PN [3] and HiFi-Net [22] that demonstrates SoTA results in attributing different forgery methods, which can be used to decide if two images are generated from the same GM. Specifically, we train HiFi-Net to classify 125 GMs and take learned features from the last fully-connected layer for the coordinated attacks detection. The performance is reported in Tab. 5a. We observe the HiFi-Net performs much worse on AUC than the model parsing baseline (*e.g.*, LGPN *w/o* pooling) and FEN-PN. Tab. 5b shows the FEN-PN and LGPN perform comparably as HiFi-Net on seen GMs (first two bar charts), yet much better than HiFi-Net when images are generated by unseen GMs (last three bar charts). Lastly, LGPN has a better Pd@5% performance than other methods.

4.4 Image Attribution

Tab. 5c reports the image attribution performance. Details can be found in Sec. 3.4. Following the previous work [3], we train our proposed dual-branch feature extractor on 100,000 real and 100,000 images generated from 4 different GMs. Our proposed method achieves the best image attribution performance on CelebA and competitive results on LSUN, indicating that our proposed dual-branch feature extractor has a promising ability to capture the generation trace.

5 Conclusion

In this study, we propose a novel method that incorporates a learnable pooling-unpooling mechanism for the model parsing. In addition, we provide a dual-branch feature extractor to help detect generation artifacts, which proves effective in three different image forensic applications.

Tracing Hyperparameter Dependencies for Model Parsing via Learnable Graph Pooling Network

– Supplementary –

Xiao Guo, Vishal Asnani, Sijia Liu, Xiaoming Liu

Michigan State University
{guoxia11, asnanivi, liusiji5, liuxm}@msu.edu

In this supplementary, we provide:

- ◇ Predictable hyperparameters introduction.
- ◇ Training and implementation details.
- ◇ Additional results of model parsing and CNN-generated image detection.
- ◇ The construction of RED140 dataset.
- ◇ Hyperparameter ground truth and the model parsing performance for each GM

1 Predictable Hyperparameters Introduction

In this study, we investigate 37 hyperparameters that exhibit the predictability according to Asnani *et al.* [3]. These hyperparameters are categorized into three groups: (1) Loss Function (Tab. 1), (2) Discrete Architecture Hyperparameters (Tab. 2), (3) Continuous Architecture Hyperparameters (Tab. 3). We report our proposed method performance of parsing hyperparameters in these three groups via Fig. 1a, Fig. 1b, and Fig. 1c, respectively. Moreover, in the main paper’s Eq. 9 and Fig. 4a, we employ the assignment hierarchy \mathbf{M}^s to group different hyperparameters together, which supervises the learning of the matching matrix \mathbf{M} . The construction of such the \mathbf{M}^s is also based on Tab. 1, 2, and 3, which not only define three coarse-level categories, but also fine-grained categories such as pixel-level objective (loss) function (*e.g.*, L1 and MSE) in Tab. 1, and normalization methods (*e.g.*, ReLU and Tanh) as well as nonlinearity functions (*e.g.*, Layer Norm. and Batch Norm.) in Tab. 2.

2 Training and Implementation Details

Training Details Given the directed graph $\mathbf{A} \in \mathbb{R}^{C \times C}$, which contains C graph nodes. We empirically set C as 55, as mentioned in the main paper Sec. 3.3. In the training, LGPN takes the given image \mathbf{I} and output the refined feature $\mathbf{V} \in \mathbb{R}^{55 \times D}$, which contains learned features for each graph node, namely, $\mathbf{V} = \{\mathbf{v}_0, \mathbf{v}_1, \dots, \mathbf{v}_{54}\}$. As a matter of fact, we can view \mathbf{V} as three separate sections: $\mathbf{V}^l = \{\mathbf{v}_0, \mathbf{v}_1, \dots, \mathbf{v}_9\}$, $\mathbf{V}^d = \{\mathbf{v}_{10}, \mathbf{v}_{11}, \dots, \mathbf{v}_{27}\}$, and $\mathbf{V}^c = \{\mathbf{v}_{28}, \mathbf{v}_{29}, \dots, \mathbf{v}_{54}\}$, which denote learned features for graph nodes of 10 loss functions (*e.g.*, L1 and MSE), 18 discrete architecture hyperparameter (*e.g.*, Batch Norm. and ReLU), and

Table 1: Loss Function types used by all GMs. We group the 10 loss functions into three categories. We use the binary representation to indicate the presence of each loss type in training the respective GM.

Category	Loss Function
Pixel-level	L_1
	L_2
	Mean squared error (MSE)
	Maximum mean discrepancy (MMD)
Discriminator	Least squares (LS)
	Wasserstein loss for GAN (WGAN)
	Kullback–Leibler (KL) divergence
	Adversarial
Classification	Hinge
	Cross-entropy (CE)

9 continuous architecture hyperparameter (*i.e.*, **Parameter Num.**), respectively. Note \mathbf{V}^c represents learned features of 9 continuous architecture hyperparameters because each continuous hyperparameter is represented by 3 graph nodes, as illustrated in Fig. 1c of the main paper.

Furthermore, via Eq. 8 in the main paper, we use \mathbf{V} to obtain the corresponding probability score $\mathbf{p} = \{p_0, p_1, \dots, p_{54}\}$ for each graph node. Similar to \mathbf{V} , this \mathbf{p} can be viewed as three sections: $\mathbf{p}^l \in \mathbb{R}^{10}$, $\mathbf{p}^d \in \mathbb{R}^{18}$ and $\mathbf{p}^c \in \mathbb{R}^{27}$ for loss functions, discrete architecture hyperparameters, continuous architecture hyperparameters, respectively. In the end, we use \mathbf{p} to help optimize LGPN via the graph node classification loss (Eq. 8). After the training converges, we further apply individual fully connected layers on the top of frozen learned features of continuous architecture hyperparameters (*e.g.*, \mathbf{V}^c), via minimizing the \mathcal{L}_1 distance between predicted and ground truth value.

In the inference (the main paper Fig. 4b), for loss function and discrete architecture hyperparameters, we use output probabilities (*e.g.*, \mathbf{p}^l and \mathbf{p}^d) of discrete value graph nodes, for the binary “used v.s. not” classification. For the continuous architecture hyperparameters, we first concatenate learned features of corresponding graph nodes. We utilize such a concatenated feature with pre-trained, fully connected layers to estimate the continuous hyperparameter value.

Implementation Details Denote the output feature from the dual-branch feature extractor as $\mathbf{f} \in \mathbb{R}^{2048}$. To transform \mathbf{f} into a set of features $\mathbf{H} = \{\mathbf{h}_0, \mathbf{h}_1, \dots, \mathbf{h}_{54}\}$ for the 55 graph nodes, 55 independent linear layers (Θ) are employed. Each feature \mathbf{h}_i is of dimension \mathbb{R}^{128} . The \mathbf{H} is fed to the GCN refinement block, which contains 5 GCN blocks, each of which has 2 stacked GCN layers. In other words, the GCN refinement block has 10 layers in total. We use the correlation graph $\mathbf{A} \in \mathbb{R}^{55 \times 55}$ (Fig. 2) to capture the hyperparameter dependency and during the training the LGPN pools \mathbf{A} into $\mathbf{A}_1 \in \mathbb{R}^{18 \times 18}$ and $\mathbf{A}_2 \in \mathbb{R}^{6 \times 6}$ as the Fig. 2 of the main paper. The LGPN is implemented using the PyTorch framework. During training, a learning rate of $3e-2$ is used. The

Table 2: Discrete Architecture Hyperparameters used by all GMs. We group the 18 discrete architecture hyperparameters into 6 categories. We use the binary representation to indicate the presence of each hyperparameter type in training the respective GM.

Category	Discrete Architecture Hyperparameters
Normalization	Batch Normalization Instance Normalization Adaptive Instance Normalization Group Normalization
Nonlinearity in the Last Layer	ReLU Tanh Leaky_ReLU Sigmoid SiLU
Nonlinearity in the Last Block	ELU ReLU Leaky_ReLU Sigmoid SiLU
Up-sampling	Nearest Neighbour Up-sampling Deconvolution
Skip Connection	Feature used
Down-sampling	Feature used

training is performed with a batch size of 400, where 200 images are generated by various GMs and 200 images are real. To enhance learning the high-resolution representation to capture generation artifacts, we increase the learning rate on the high-res branch as $5e-2$. We use `ReduceLROnPlateau` as the scheduler to adjust the learning rate based on the validation loss.

3 Additional Results

Tab. 1 of the main paper and Tab. 5 of the supplementary report the model parsing performance on RED140 and RED116, respectively. As demonstrated by these two tables, our proposed LGPN achieves the best performance on both datasets.

In Fig. 5 of the main paper, we visualize the correlation graph similarities among different GMs in the first test set. In this section, we offer a similar visualization (*e.g.*, Fig. 3 of the supplementary) for other test sets. Supplementary’s Fig. 4 shows the relationship between graph node classification and GM correlation graph similarity for GMs. In the main paper’s Sec 3.4, we use n graph nodes for each continuous hyperparameter and n is set as 3. Tab. 4 shows the advantage of choice, which shows the lowest \mathcal{L}_1 regression error is achieved when n is 3.

Furthermore, in addition to Tab. 3 and 4 of the main paper, we provide the CNN-generated image detection performance measured by Accuracy in Supplementary’s Tab. 7 and 8.

Table 3: Continuous Architecture Hyperparameters used by all GMs, where "[" denotes inclusive and "(" denotes exclusive intervals. We report the range for 9 continuous hyperparameters.

Category	Range	Discrete Architecture Hyperparameters
Layer Number	(0—717]	Layers Number
	[0—289]	Convolution Layer Number
	[0—185]	Fully-connected Layer Number
	[0—46]	Pooling Layer Number
	[0—235]	Normalization Layer Number
	(0—20]	Layer Number per Block
Unit Number	(0—8, 365]	Filter Number
	(0—155]	Block Number
	(0—56, 008, 488]	Parameter Number

Table 4: Using different n graph nodes for the continuous hyperparameter regression.

n Value	2	3	4	5	6
L1 Error	0.108	0.105	0.106	0.112	0.120

4 RED140 Dataset

In this section, we provide an overview of the RED140 dataset, which is used for both model parsing and coordinated attack detection. Note that, for the experiment reported in Tab. 5 of the supplementary, we follow the test sets defined in RED116 [3]. When we construct RED140, we use images from ImageNet, FFHQ, CelebHQ, CIFAR10 and LSUN as the real-images category of RED140, and exclude GM that is not trained on the real-image category of RED140. In addition, both RED116 and RED140 contain various image content and resolution, and the details about RED140 are uncovered in Fig. 5 of the supplementary. For test sets (Tab. 6 of the supplementary), we follow the dataset partition of RED116, excluding the GMs that are trained on real images, which RED140 does have. For example, JFT-300M is used to train BigGAN, so we remove BIGGAN_128, BIGGAN_256 and BIGGAN_512 in the first, second and third test sets.

5 GM Hyperparameter Ground Truth

In this section, we report the ground truth vector of different hyperparameters of each GM contained in the RED140. Specifically, Tab. 9 and Tab. 10 report the loss function ground truth vector for each GM. Tab. 11 and Tab. 12 report the discrete architecture hyperparameter ground truth for each GM. Tab. 13 and Tab. 14 report the discrete architecture hyperparameter ground truth for each GM. The detailed model parsing performance on each GM is reported in the supplementary’s Fig. 6.

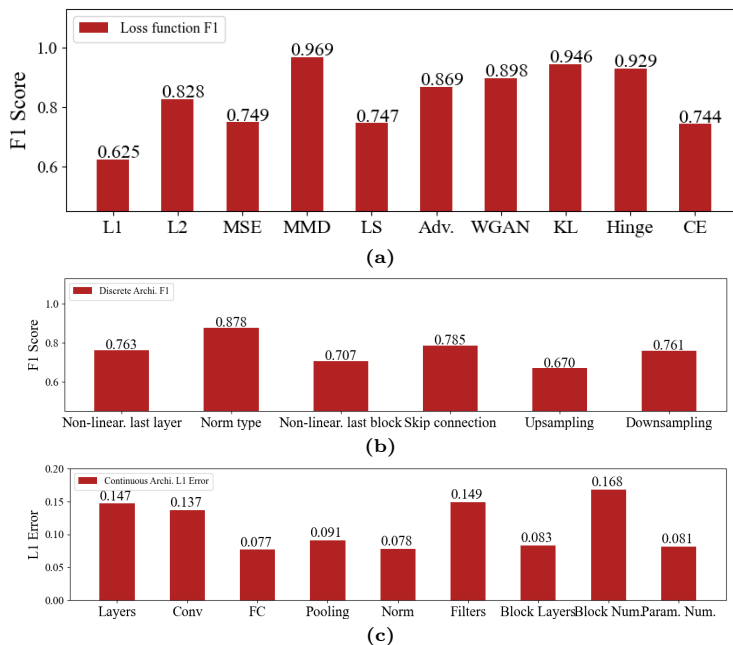


Fig. 1: (a) The F1score on the loss function reveals that MMD and KL are two easiest loss functions to predict. (b) The F1score on the discrete architecture hyperparameters demonstrates that predicting these hyperparameters is more challenging than predicting the loss function. This finding aligns with the empirical results reported in the previous work [3]. (c) The L1 error on the continuous architecture hyperparameters indicates that it is challenging to predict Block Num. and Filter Num..

Method	Loss Function		Dis. Archi. Para.		Con. Archi. Para.
	F1 \uparrow	Acc. \uparrow	F1 \uparrow	Acc. \uparrow	L1 error \downarrow
Random GT [3]	0.636	0.716	0.529	0.575	0.184
FEN [3]	0.813	0.792	0.718	0.706	0.149
FEN.* [3]	0.801	0.811	0.701	0.708	0.146
DB feat. <i>w</i> MLP	0.778	0.801	0.689	0.701	0.169
DB feat. <i>w</i> Stacked GCN	0.790	0.831	0.698	0.720	0.145
DB feat. <i>w</i> GCN refine.	0.841	0.833	0.727	0.755	0.130

Table 5: The model parsing performance on RED116. In the last row, our proposed LGPN that contains DB feat. and GCN refinement block, which achieves the best model parsing performance in all metrics. [Key: DB feat.: dual-branch feature extractor; GCN refine.: GCN refinement block; **Bold**: best.].

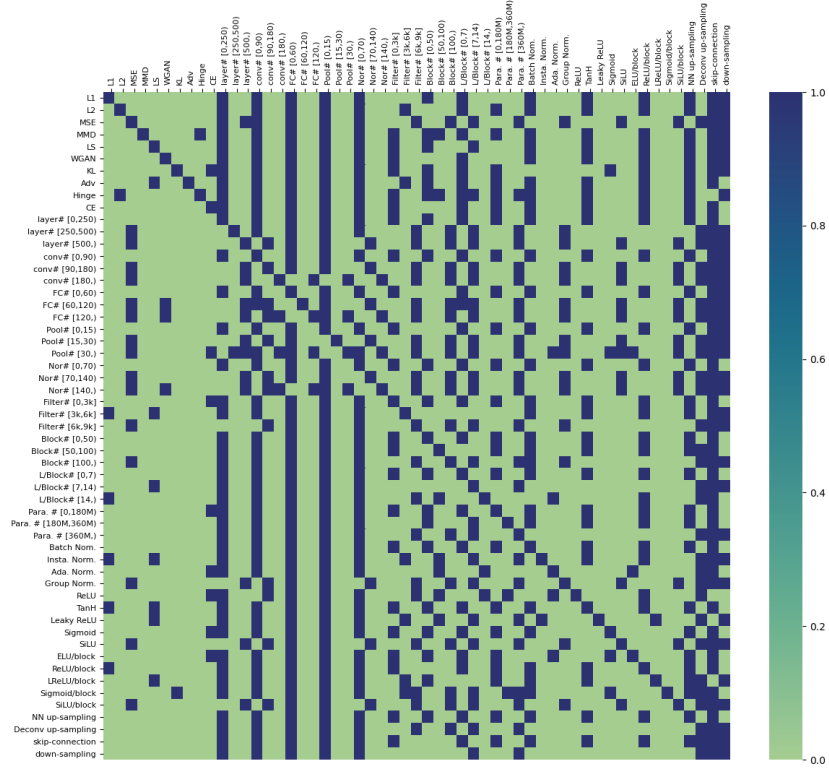


Fig. 2: The initial correlation graph \mathbf{A} that we construct based on the probability table in Sec. 3.1 of the main paper. The optimum threshold we use is 0.45.

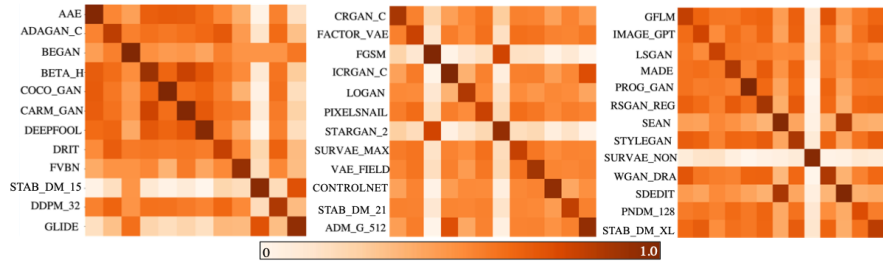


Fig. 3: Each element of these two matrices is the average cosine similarities of 2,000 pairs of generated correlation graphs \mathbf{A}'_0 from corresponding GMs in the second, third and fourth test sets.

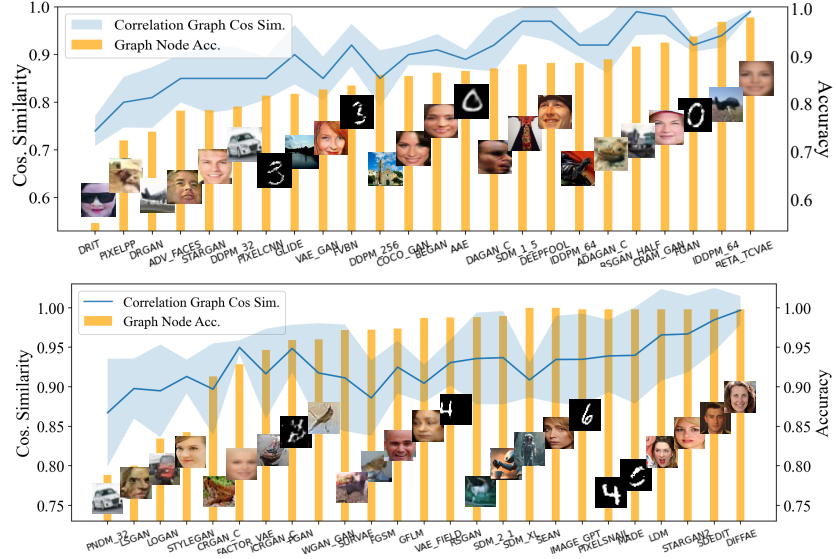


Fig. 4: For each GM in four test sets. The upper figure corresponds to the first and second test sets, while the lower figure corresponds to the third and fourth test sets. The positive correlation between the cosine similarity between image pairs’ correlation graphs (*i.e.*, A'_0) and the graph node classification accuracy achieved by LGPN on that particular GM. This positive correlation demonstrates that the correlation graph is important to the performance of the graph node classification, which encourages the LGPN to learn the representation for each hyperparameter.

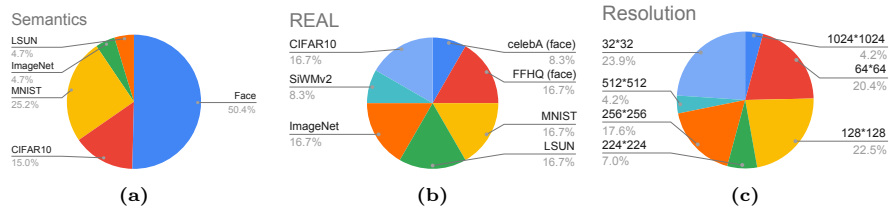


Fig. 5: RED140 statistics. (a) The dataset is trained on various image contents or semantics. (b) The real-image category contains many real-image datasets that GMs are trained on [14, 23, 31, 32, 35, 36, 63]. (c) The GM has various image resolutions.

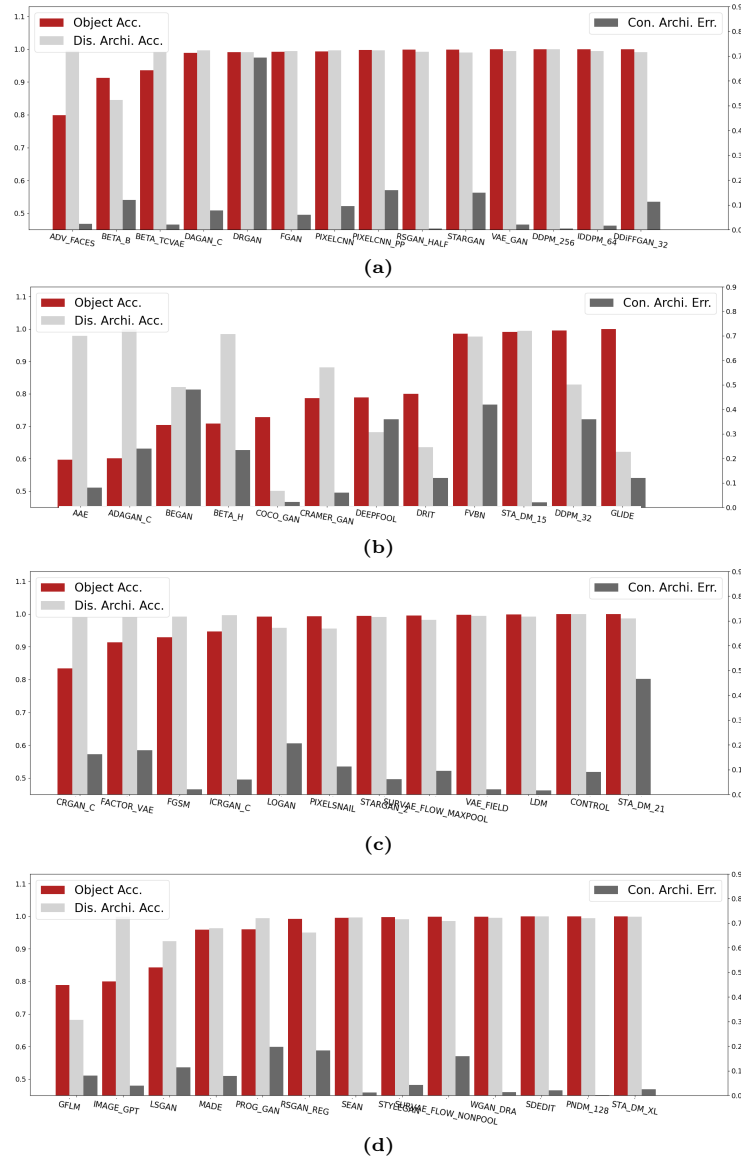


Fig. 6: We report detailed model parsing results on different GMs in each test set. These results include loss function and discrete architecture hyperparameter prediction accuracy, as well as the L1 error on the continuous architecture hyperparameter prediction. Specifically, (a), (b), (c), and (d) are the performance for GMs in the 1st, 2nd, 3rd and 4th test sets, respectively.

Table 6: Test sets used for evaluation. Each set contains generative models from GAN, DM, VAE, AR (Auto-Regressive), AA (Adversarial Attack) and NF (Normalizing Flow). All test sets contain face and non-face in the image content. [Keys: R means GM is used in the test set of RED116 but is not used in RED140.]

Set 1	Set 2	Set 3	Set 4
ADV_FACES	AAE	BICYCLE_GAN (R)	GFLM
BETA_B	ADAGAN_C	BIGGAN_512 (R)	IMAGE_GPT
BETA_TCVAE	BEGAN	CRGAN_C	LSGAN
BIGGAN_128 (R)	BETA_H	FACTOR_VAE	MADE
DAGAN_C	BIGGAN_256 (R)	FGSM	PIX2PIX (R)
DRGAN	COCOGEN	ICRGAN_C	PROG_GAN
FGAN	CRAMERGAN	LOGAN	RSGAN_REG
PIXEL_CNN	DEEPFOOL	MUNIT (R)	SEAN
PIXEL_CNN++	DRIT	PIXEL_SNAIL	STYLE_GAN
RSGAN_HALF	FAST_PIXEL(R)	STARGAN_2	SURVAE_FLOW_NONPOOL
STARGAN	FVBN	SURVAE_FLOW_MAXPOOL	WGAN_DRA
VAEGAN	SRFLOW (R)	VAE_FIELD	YLG (R)
DDPM_256	STABLE_DM_21	LDM	PNDM_32
IDDPM_64	DDPM_32	CONTROLNET	STABLE_DM_XL
Denoise_GAN_32	GLIDE	STABLE_DM_15	SEDdit

Detection method	Variant	Generative Adversarial Networks						Deepfakes		Low level vision			Perceptual loss		Average
		Pro-GAN	Cycle-GAN	Big-GAN	Style-GAN	Gau-GAN	Star-GAN	FF++	SITD	SAN	CRN	IMLE			
Trained network [57]	Blur+JPEG (0.1)	99.90	85.20	70.20	85.70	78.95	91.70	53.47	66.67	48.69	86.31	86.26	77.46		
	Blur+JPEG (0.5)	100.0	80.77	58.98	69.24	79.25	80.94	51.06	56.94	47.73	87.58	94.07	73.32		
	ViT:CLIP (0.5)	98.94	78.80	60.62	60.56	66.82	62.31	52.28	65.28	47.97	64.09	80.00	67.02		
Patch classifier [5]	ResNet50-Layer1	94.38	67.38	64.62	82.26	57.19	80.29	55.32	64.59	51.24	54.29	55.11	66.06		
	Xception-Block2	75.03	68.97	68.47	79.16	64.23	63.94	75.54	75.00	75.00	72.00	55.52	70.31		
Co-occurrence [44]	-	97.70	63.15	53.75	92.50	51.10	54.70	57.10	63.00	58.02	65.65	66.00	65.49		
Freq-spec [68]	CycleGAN	49.90	99.99	50.50	49.90	50.30	99.70	50.10	50.00	48.00	51.00	50.00	59.00		
Universal detector [47]	NN, $k=1$	99.58	94.70	86.95	80.24	96.67	98.84	80.90	71.00	56.00	66.00	77.10	82.52		
	LC	100.0	98.50	94.50	82.00	99.50	97.00	66.60	63.00	58.00	60.00	72.00	81.00		
Ours		100.0	93.75	94.60	97.02	94.93	99.92	52.76	90.27	52.96	98.16	98.28	88.02		

Table 7: CNN-generated image detection performance measured by Accuracy on 11 forgery methods containing face and non-face images. Previous methods’ quantitative results are taken from [47]. [**Red**: best result; **Blue**: second best result].

Detection method	Deep fakes Celeb-DF	Diffusion models				Commercial			Average
		DD-PM	DD-IM	GLIDE	LDM	DALL-E2	Mid Jour.	SORA	
ResNet (0.1) [57]	87.20	70.53	68.71	66.64	77.75	70.80	53.13	50.25	68.13
ResNet (0.5) [57]	82.00	68.03	65.33	69.03	72.11	71.31	61.37	54.18	67.20
Universal detector [47]	60.31	89.55	91.00	90.00	89.77	95.77	58.21	65.11	79.97
DIRE [58]	74.55	82.41	78.17	83.94	86.81	75.00	52.49	52.11	73.19
Ours	89.20	90.4	90.30	94.2	84.70	90.10	55.88	64.42	82.40

Table 8: CNN-generated image detection performance by accuracy on images generated via deepfakes (*e.g.*, Celeb-DF [40]), diffusion models (10k images for each category), and commercial softwares. [**Red**: best result].

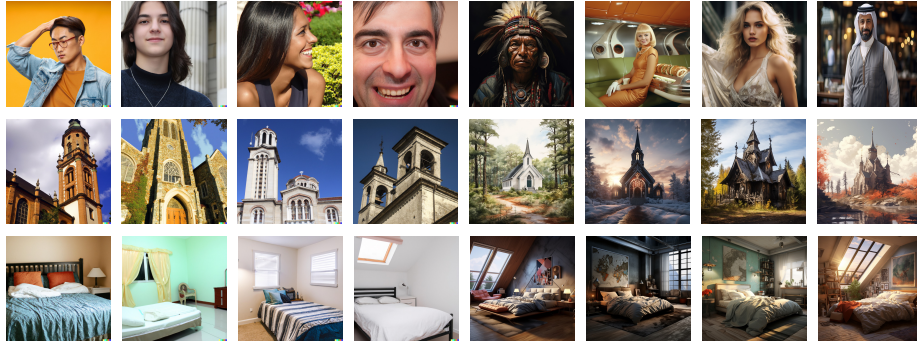


Fig. 7: Collected images from DALL-E2 and Midjourney. From top to down, different rows represent different image categories: person, bedroom, and church. In each row, the first and last 4 images are from DALL-E2 and Midjourney, respectively.

Table 10: Ground truth Loss Function feature vector used for prediction of loss type for all GMs. The loss function ground truth is in (Tab. 1).

GM	L_1	L_2	MSE	MMD	LS	WGAN	KL	Adversarial	Hinge	CE
IDDPM_32	0	0	1	0	0	0	0	0	0	0
IDDPM_64	0	0	1	0	0	0	0	0	0	0
IDDPM_256	0	0	1	0	0	0	0	0	0	0
ILVER_256	0	0	1	0	0	0	0	0	0	0
Image_GPT	0	0	0	0	0	0	0	0	0	1
INFOGAN	0	0	1	0	1	0	0	0	0	1
LAPGAN	0	0	0	0	1	0	0	0	0	0
LDM	0	0	1	0	0	0	0	0	0	0
LDM_CON	0	0	1	0	0	1	0	0	0	0
Lmconv	0	0	0	0	0	0	0	0	0	1
LOGAN	1	1	0	0	0	0	0	1	0	0
LSGAN	0	0	1	0	0	0	0	0	1	0
MADE	0	0	0	0	0	0	0	0	0	1
MAGAN	0	0	1	0	0	0	0	0	0	0
MEMGAN	0	0	0	0	1	0	0	0	0	0
MMD_GAN	1	0	0	1	0	0	0	0	0	0
MORGAN	0	0	1	0	1	0	0	0	0	0
MSG_STYLE_GAN	0	0	0	0	1	0	0	0	0	0
MUNIT	1	0	0	0	1	0	0	0	0	0
NADE	0	0	0	0	0	0	0	0	0	1
OCFGAN	0	0	0	1	0	0	0	0	1	0
PGD	1	1	0	0	0	0	0	0	0	0
PIX2PIX	1	0	0	0	1	0	0	0	0	0
PixelCNN	0	0	0	0	0	0	0	0	0	1
PixelCNN++	0	0	0	0	0	0	0	0	0	1
PIXELDA	0	0	0	0	1	0	0	0	1	1
PixelSnail	0	0	0	0	0	0	0	0	0	1
PNDM_32	0	0	1	0	0	0	0	0	0	0
PNDM_256	0	0	1	0	0	0	0	0	0	0
PROG_GAN	0	0	0	0	0	1	0	0	1	0
RGAN	0	0	0	0	0	1	0	0	0	0
RSGAN_HALF	0	0	0	0	0	0	0	0	0	1
RSGAN_QUAR	0	0	0	0	0	0	0	0	0	1
RSGAN_REG	0	0	0	0	0	0	0	0	0	1
RSGAN_RES_BOT	0	0	0	0	0	0	0	0	0	1
RSGAN_RES_HALF	0	0	0	0	0	0	0	0	0	1
RSGAN_RES_QUAR	0	0	0	0	0	0	0	0	0	1
RSGAN_RES_REG	0	0	0	0	0	0	0	0	0	1
SAGAN	0	0	0	0	1	0	0	0	0	0
SCOREDIFF_256	0	0	1	0	0	0	0	0	0	0
SDEdit_256	0	0	1	0	0	0	0	0	0	0
SEAN	1	0	0	0	1	0	0	0	0	0
SEMANTIC	0	1	0	0	1	0	0	0	0	0
SGAN	0	0	0	0	1	0	0	0	0	1
SNGAN	0	0	0	0	1	0	0	1	0	0
SOFT_GAN	0	0	0	0	1	0	0	0	0	0
SRFLOW	1	0	0	0	0	0	0	0	0	1
SRRNET	0	1	1	0	1	0	0	0	0	1
STANDARD_VAE	0	0	0	0	0	0	1	0	0	1
STARGAN	1	0	0	0	1	0	0	0	0	1
STARGAN_2	1	0	0	0	1	0	0	0	0	0
STA_DM_15	0	0	1	0	0	0	0	0	0	0
STA_DM_21	0	0	1	0	0	0	0	0	0	0
STA_DM_XL	0	0	1	0	0	0	0	0	0	0
STGAN	1	0	0	0	1	1	0	0	0	0
STYLEGAN	0	1	0	0	0	1	0	0	0	0
STYLEGAN_2	0	1	0	0	1	0	0	0	1	0
STYLEGAN2_ADA	0	1	0	1	1	0	0	0	1	0
SURVAE_FLOW_MAXPOOL	0	0	0	0	0	0	1	0	0	1
SURVAE_FLOW_NONPOOL	0	0	0	0	0	0	1	0	0	1
TPGAN	1	0	0	0	0	1	0	0	0	0
UGAN	0	0	0	0	1	0	0	0	0	0
UNIT	0	0	0	0	1	0	1	0	0	0
VAE_field	0	0	0	0	0	0	1	0	0	1
VAE_flow	0	0	0	0	0	0	1	0	0	1
VAEGAN	1	0	0	0	1	0	1	0	0	0
VDVAE	0	0	0	0	0	0	1	0	0	1
WGAN	0	0	0	0	0	1	0	0	0	0
WGAN_DRA	0	0	1	0	0	1	0	0	0	0
WGAN_WC	0	0	0	0	0	1	0	0	0	0
WGANP	0	1	0	0	0	1	0	0	0	0
YLG	0	0	0	0	0	1	0	0	0	0

Table 11: Ground truth feature vector used for prediction of Discrete Architecture Hyperparameters for all GMs. The discrete architecture hyperparameter ground truth is defined in (Tab. 2). **A — D** are Batch Norm., Instance Norm., Adaptive Instance Norm., and Group Norm., respectively. **E — I** are non-linearity in the last layer, and they are ReLU, Tanh, Leaky_ReLu, Sigmoid, and SiLU. **J — N** are non-linearity in the last block, and they are ELU, ReLU, Leaky_ReLu, Sigmoid, and SiLU. **O** and **P** are Nearest Neighbour and Deconvolution Upsampling. **Q** and **L** are Skip Connection and Downsampling.

GM	A	B	C	D	E	F	G	H	I	J	K	L	M	N	O	P	Q	L		
AAE	1	0	0	0	1	0	0	0	1	0	0	0	0	1	0	1	0	1	0	
ACGAN	1	0	0	0	0	1	0	0	0	0	1	0	0	0	0	1	0	1	0	
ADAGAN_C	1	0	0	0	0	1	0	0	0	0	1	0	0	0	0	1	0	1	0	
ADAGAN_P	1	0	0	0	0	1	0	0	0	0	1	0	0	0	0	1	0	1	0	
ADM_G_128	0	0	0	1	0	0	0	0	0	1	0	0	0	0	1	0	1	1	1	
ADM_G_256	0	0	0	1	0	0	0	0	0	1	0	0	0	0	1	0	1	1	1	
ADV_FACES	0	1	0	0	0	1	0	0	0	0	1	0	0	0	0	1	0	1	0	
ALAE	0	1	0	0	0	0	1	0	0	0	0	1	0	0	0	1	0	1	1	
BEGAN	1	0	0	0	0	1	0	0	0	1	0	0	0	0	0	1	0	0	0	
BETA_B	0	0	0	0	0	0	0	1	0	0	1	0	0	0	0	1	0	1	1	
BETA_H	0	0	0	0	0	0	0	1	0	0	1	0	0	0	0	1	0	1	1	
BETA_TCVAE	0	0	0	0	0	0	0	1	0	0	1	0	0	0	0	1	0	1	1	
BGAN	1	0	0	0	0	1	0	0	0	0	0	0	1	0	0	1	0	0	0	
BICYCLE_GAN	1	0	0	0	0	1	0	0	0	0	1	0	0	0	0	1	0	0	0	
BIGGAN_128	1	0	0	0	0	1	0	0	0	0	1	0	0	0	0	0	1	1	1	
BIGGAN_256	1	0	0	0	0	1	0	0	0	0	1	0	0	0	0	0	1	1	1	
BIGGAN_512	1	0	0	0	0	1	0	0	0	0	1	0	0	0	0	0	0	1	1	1
Blended_DM	0	0	0	1	0	0	0	0	1	0	0	0	0	0	1	0	1	1	1	
CADGAN	1	0	0	0	0	1	0	0	0	0	1	0	0	0	0	1	0	1	1	
CCGAN	1	0	0	0	0	1	0	0	0	0	1	0	0	0	0	0	1	1	1	
CGAN	1	0	0	0	0	1	0	0	0	0	0	0	1	0	0	1	0	0	0	
CLIPDM	0	0	0	1	0	0	0	0	0	0	0	0	0	0	0	0	1	1	1	
COCO_GAN	1	0	0	0	0	1	0	0	0	0	1	0	0	0	0	1	0	0	0	
COGAN	1	0	0	0	0	1	0	0	0	0	0	1	0	0	0	1	0	1	1	
COLOUR_GAN	1	0	0	0	0	1	0	0	0	0	1	0	0	0	0	1	0	1	1	
CONT_ENC	1	0	0	0	0	1	0	0	0	0	0	1	0	0	0	1	0	1	1	
CONTRAGAN	1	0	0	0	0	1	0	0	0	0	1	0	0	0	0	1	0	1	0	
CONTROLNET	0	0	0	1	0	0	0	0	0	1	0	0	0	0	1	0	1	1	0	
COUNCIL_GAN	0	1	0	0	0	1	0	0	0	0	1	0	0	0	0	1	0	1	0	
CRAMER_GAN	1	0	0	0	0	1	0	0	0	0	1	0	0	0	0	1	0	1	0	
CRGAN_C	1	0	0	0	0	1	0	0	0	0	1	0	0	0	0	1	0	1	0	
CRGAN_P	1	0	0	0	0	1	0	0	0	0	1	0	0	0	0	1	0	1	0	
CYCLEGAN	0	1	0	0	0	1	0	0	0	0	1	0	0	0	0	0	1	1	1	
DAGAN_C	1	0	0	0	0	1	0	0	0	0	1	0	0	0	0	1	0	1	0	
DAGAN_P	1	0	0	0	0	1	0	0	0	0	1	0	0	0	0	1	0	1	0	
DCGAN	1	0	0	0	0	1	0	0	0	0	1	0	0	0	0	1	0	1	0	
DDiFFGAN_32	0	0	0	1	0	0	0	0	0	1	0	0	0	0	1	0	1	1	1	
DDPM_32	0	0	0	1	0	0	0	0	0	0	0	0	0	0	0	0	1	1	1	
DDPM_256	0	0	0	1	0	0	0	0	0	0	0	0	0	0	0	0	1	1	1	
DEEPPFOOL	0	0	1	0	1	0	0	0	0	0	1	0	0	0	0	0	1	0	0	
DFCVAE	1	0	0	0	0	0	0	1	0	0	0	1	0	0	0	1	0	0	1	
DIFF_ISGEN	1	0	0	0	0	0	0	1	0	0	0	0	1	0	0	1	1	0	0	
DIFF_PGAN	1	0	0	0	0	0	0	1	0	0	0	0	1	0	0	1	1	0	0	
DIFF_SGAN	1	0	0	0	0	0	0	1	0	0	0	0	1	0	0	1	1	0	0	
DIFFFAE	0	0	0	1	0	0	0	0	1	0	0	0	0	1	0	0	1	1	1	
DIFFFAE_LATENT	0	0	0	1	0	0	0	0	1	0	0	0	0	1	0	0	1	1	1	
DISCOGAN	0	1	0	0	0	1	0	0	0	0	0	1	0	0	0	0	1	1	1	
DRGAN	1	0	0	0	0	1	0	0	0	1	0	0	0	0	0	1	0	1	1	
DRIT	0	1	0	0	0	1	0	0	0	0	1	0	0	0	0	0	1	1	1	
DUALGAN	1	0	0	0	0	1	0	0	0	0	1	0	0	0	0	1	0	0	0	
EBGAN	1	0	0	0	0	1	0	0	0	0	0	1	0	0	0	1	0	0	1	
ESRGAN	0	0	1	0	0	0	0	1	0	0	0	0	1	0	0	0	1	0	0	
FACTOR_VAE	0	0	0	0	0	0	0	1	0	0	1	0	0	0	0	1	0	1	1	
FASTPIXEL	1	0	0	0	0	0	0	1	0	1	0	0	0	0	0	1	0	1	0	
FFGAN	1	0	0	0	0	1	0	0	0	0	1	0	0	0	0	1	1	1	1	
FGAN	1	0	0	0	0	0	0	1	0	0	1	0	0	0	0	1	0	1	0	
FGAN_KL	1	0	0	0	0	0	0	1	0	0	1	0	0	0	0	1	0	1	0	
FGAN_NEYMAN	1	0	0	0	0	0	0	1	0	0	1	0	0	0	0	1	0	1	0	
FGAN_PEARSON	1	0	0	0	0	0	0	1	0	0	1	0	0	0	0	1	0	1	0	
FGSM	0	0	1	0	1	0	0	0	0	0	1	0	0	0	0	0	1	0	0	
FPGAN	0	1	0	0	0	1	0	0	0	0	1	0	0	0	0	1	0	0	1	
FSGAN	1	0	0	0	1	0	0	0	0	0	1	0	0	0	0	0	1	1	1	
FVBN	0	0	1	0	0	0	0	0	1	0	1	0	0	0	0	0	1	0	1	0
GAN_ANIME	0	1	0	0	0	1	0	0	0	0	1	0	0	0	0	0	1	0	1	1
GATED_PIXEL_CNN	0	0	1	0	0	0	0	0	1	0	0	0	1	0	0	0	0	1	1	0
GDWCT	0	1	0	0	0	1	0	0	0	0	1	0	0	0	0	1	0	0	1	0
GFLM	0	0	1	0	1	0	0	0	0	0	1	0	0	0	0	0	1	0	0	0
GGAN	1	0	0	0	0	1	0	0	0	0	1	0	0	0	0	1	0	1	1	1
GLIDE	0	0	0	1	0	0	0	0	1	0	0	0	0	0	1	0	1	1	1	1

Table 12: Ground truth feature vector used for prediction of Discrete Architecture Hyperparameters for all GMs. The discrete architecture hyperparameter ground truth is defined in (Tab. 2). **A — D** are Batch Norm., Instance Norm., Adaptive Instance Norm., and Group Norm., respectively. **E — I** are non-linearity in the last layer and they are ReLU, Tanh, Leaky_ReLu, Sigmoid, and SiLU. **J — N** are non-linearity in the last block and they are ELU, ReLU, Leaky_ReLu, Sigmoid, and SiLU. **O** and **P** are Nearest Neighbour and Deconvolution Upsampling. **Q** and **L** are Skip Connection and Downsampling.

GM	A	B	C	D	E	F	G	H	I	J	K	L	M	N	O	P	Q	L
ICRGAN_C	1	0	0	0	0	1	0	0	0	0	1	0	0	0	1	0	1	0
ICRGAN_P	1	0	0	0	0	1	0	0	0	0	1	0	0	0	1	0	1	0
IDDPM_32	0	0	0	1	0	0	0	0	1	0	0	0	0	0	1	0	1	1
IDDPM_64	0	0	0	1	0	0	0	0	1	0	0	0	0	0	1	0	1	1
IDDPM_256	0	0	0	1	0	0	0	0	1	0	0	0	0	0	1	0	1	1
IMAGE_GPT	1	0	0	0	0	0	0	1	0	0	0	1	0	0	0	1	1	1
INFOGAN	1	0	0	0	0	1	0	0	0	0	0	1	0	0	1	0	0	1
ILVER_256	0	0	0	1	0	0	0	0	0	0	0	0	0	0	0	1	1	1
LAPGAN	0	0	1	0	0	1	0	0	0	0	1	0	0	0	0	0	1	1
LDM	0	0	0	1	0	0	0	0	1	0	0	0	0	1	0	1	1	1
LDM_CON	0	0	0	1	0	0	0	0	1	0	0	0	0	1	0	1	1	1
LMCONV	0	0	1	0	0	0	0	1	0	1	0	0	0	0	0	1	1	1
LOGAN	1	0	0	0	0	1	0	0	0	0	1	0	0	0	1	0	1	0
LSGAN	1	0	0	0	0	1	0	0	0	0	1	0	0	0	1	0	0	0
MADE	0	0	1	0	0	0	0	1	0	1	0	0	0	0	0	1	0	1
MAGAN	1	0	0	0	0	1	0	0	0	0	1	0	0	0	1	0	1	0
MEMGAN	1	0	0	0	0	1	0	0	0	0	1	0	0	0	1	0	1	0
MMD_GAN	1	0	0	0	0	1	0	0	0	0	1	0	0	0	1	0	1	0
MRGAN	1	0	0	0	0	1	0	0	0	0	1	0	0	0	1	0	1	0
MSG_STYLE_GAN	0	1	0	0	0	0	1	0	0	0	0	1	0	0	0	1	0	1
MUNIT	0	1	0	0	1	0	0	0	0	0	1	0	0	0	0	1	1	1
NADE	0	0	1	0	0	0	0	1	0	1	0	0	0	0	1	0	1	0
OCFGAN	1	0	0	0	0	1	0	0	0	0	1	0	0	0	1	0	1	0
PGD	0	0	1	0	1	0	0	0	0	0	1	0	0	0	0	1	0	0
PIX2PIX	0	1	0	0	0	1	0	0	0	0	0	1	0	0	0	1	1	1
PIXELCNN	1	0	0	0	0	0	0	1	0	1	0	0	0	0	1	0	1	0
PIXELCNN_PP	0	0	1	0	0	0	0	1	0	1	0	0	0	0	0	1	1	1
PIXELDA	1	0	0	0	0	1	0	0	0	0	1	0	0	0	0	1	0	0
PIXELSNAIL	0	0	1	0	1	0	0	0	0	0	0	0	1	0	1	0	1	0
PNDM_32	0	0	0	1	0	0	0	0	1	0	0	0	0	1	0	1	1	1
PNDM_256	0	0	0	1	0	0	0	0	1	0	0	0	0	1	0	1	1	1
PROG_GAN	1	0	0	0	0	0	0	1	0	0	0	0	1	0	1	0	0	1
RGAN	1	0	0	0	0	1	0	0	0	0	1	0	0	1	0	1	0	0
RSGAN_HALF	1	0	0	0	0	1	0	0	0	0	1	0	0	0	1	0	1	0
RSGAN_QUAR	1	0	0	0	0	1	0	0	0	0	1	0	0	0	1	0	1	0
RSGAN_REG	1	0	0	0	0	1	0	0	0	0	1	0	0	0	1	0	1	0
RSGAN_RES_BOT	1	0	0	0	0	1	0	0	0	0	1	0	0	0	0	1	1	0
RSGAN_RES_HALF	1	0	0	0	0	1	0	0	0	0	1	0	0	0	0	1	1	0
RSGAN_RES_QUAR	1	0	0	0	0	1	0	0	0	0	1	0	0	0	0	1	1	0
RSGAN_RES_REG	1	0	0	0	0	1	0	0	0	0	1	0	0	0	0	1	1	0
SAGAN	1	0	0	0	0	1	0	0	0	0	0	1	0	0	1	0	0	0
SCOREDIFF_256	0	0	0	1	0	0	0	0	0	0	0	0	0	0	0	1	1	1
SDEDIT	0	0	0	1	0	0	0	0	0	0	0	0	0	0	0	1	1	1
SEAN	0	0	0	0	0	1	0	0	0	0	1	0	0	0	1	0	1	0
SEMANTIC	0	1	0	0	0	1	0	0	0	0	1	0	0	0	1	0	0	1
SGAN	1	0	0	0	0	1	0	0	0	0	0	1	0	0	1	0	0	1
SGAN	1	0	0	0	0	1	0	0	0	0	0	1	0	0	1	0	1	0
SOFT_GAN	1	0	0	0	0	1	0	0	0	0	0	1	0	0	1	0	0	0
SRFLOW	0	0	1	0	0	0	1	0	0	1	0	0	0	0	0	1	0	0
SRRNET	1	0	0	0	0	1	0	0	0	0	1	0	0	0	1	0	1	1
STANDARD_VAE	0	0	0	0	0	0	0	1	0	0	1	0	0	0	1	0	1	1
STA_DM_15	0	0	0	1	0	0	0	0	1	0	0	0	0	1	0	1	1	0
STA_DM_21	0	0	0	1	0	0	0	0	1	0	0	0	0	1	0	1	1	0
STA_DM_XL	0	0	0	1	0	0	0	0	1	0	0	0	0	1	0	1	1	0
STARGAN	0	1	0	0	0	1	0	0	0	0	1	0	0	0	1	0	0	1
STARGAN_2	0	1	0	0	0	0	1	0	0	0	0	1	0	0	1	0	0	1
STGAN	1	0	0	0	0	1	0	0	0	0	1	0	0	0	1	0	1	1
STYLEGAN	0	1	0	0	0	0	1	0	0	0	0	1	0	0	0	1	0	1
STYLEGAN_2	0	1	0	0	0	0	1	0	0	0	0	1	0	0	0	1	0	1
STYLEGAN_ADA	0	1	0	0	0	0	1	0	0	0	0	1	0	0	0	1	0	1
SURVAE_M	0	0	1	0	1	0	0	0	0	1	0	0	0	0	1	0	0	0
SURVAE_N	0	0	1	0	1	0	0	0	0	1	0	0	0	0	1	0	0	0
TPGAN	1	0	0	0	0	0	0	1	0	0	0	0	1	0	1	0	1	1
UGAN	1	0	0	0	0	0	0	1	0	0	1	0	0	0	1	0	1	0
UNIT	0	1	0	0	0	0	1	0	0	0	1	0	0	0	0	1	1	1
VAE_FIELD	0	0	1	0	0	0	0	1	0	1	0	0	0	0	1	0	0	0
VAE_FLOW	0	0	1	0	0	0	0	1	0	1	0	0	0	0	1	0	0	0
VAE_GAN	1	0	0	0	0	1	0	0	0	0	1	0	0	0	1	0	0	1
VDVAE	0	0	1	0	1	0	0	0	0	0	0	1	0	0	0	1	1	1
WGAN	1	0	0	0	0	1	0	0	0	0	1	0	0	0	1	0	0	0
WGAN_DRA	1	0	0	0	0	1	0	0	0	0	1	0	0	0	1	0	1	0
WGAN_WC	1	0	0	0	0	1	0	0	0	0	1	0	0	0	1	0	1	0
WGAN_WC	1	0	0	0	0	1	0	0	0	0	1	0	0	0	1	0	0	0
YLG	1	0	0	0	0	1	0	0	0	0	1	0	0	0	1	1	1	1

Table 13: Ground truth feature vector used for prediction of Continuous Architecture Hyperparameters for all GMs. The discrete architecture hyperparameter ground truth is defined in (Tab. 3). F1: # layers, F2: # convolutional layers, F3: # fully connected layers, F4: # pooling layers, F5: # normalization layers, F6: #filters, F7: # blocks, F8:# layers per block, and F9: # parameters.

GM	Layer #	Conv. #	FC #	Pool #	Norm. #	Filter #	Block #	Block Layer #	Para. #
AAE	9	0	7	0	2	0	0	0	1,593,378
ACGAN	18	10	1	0	7	2,307	5	3	4,276,739
ADAGAN_C	35	14	13	1	7	4,131	9	3	9,416,196
ADAGAN_P	35	14	13	1	7	4,131	9	3	9,416,196
ADM_G_128	223	90	37	8	88	N/A	34	7	421,529,606
ADM_G_256	266	107	45	11	103	N/A	39	7	553,838,086
ADV_FACES	45	23	1	1	20	2,627	4	6	30,000,000
ALAE	33	25	8	0	0	4,094	3	8	50,200,000
BEGAN	10	9	1	0	0	515	2	4	7,278,472
BETA_B	7	4	3	0	0	99	1	3	469,173
BETA_H	7	4	3	0	0	99	1	3	469,173
BETA_TCVAE	7	4	3	0	0	99	1	3	469,173
BGAN	8	0	5	0	3	0	2	3	1,757,412
BICYCLE_GAN	25	14	1	0	10	4,483	2	10	23,680,256
BIGGAN_128	63	21	1	0	41	6,123	6	10	50,400,000
BIGGAN_256	75	25	1	0	49	7,215	6	12	55,900,000
BIGGAN_512	87	29	1	0	57	8,365	6	14	56,200,000
Blended_DM	266	107	45	11	103	N/A	39	7	553,838,086
CADGAN	8	4	1	0	3	451	3	2	3,812,355
CCGAN	22	12	0	0	10	3,203	2	9	29,257,731
CGAN	8	0	5	0	3	0	2	3	1,757,412
COCO_GAN	19	9	1	0	9	2,883	3	4	50,000,000
COGAN	9	5	0	0	4	259	2	2	1,126,790
COLOUR_GAN	19	10	0	0	9	2,435	2	9	19,422,404
CONT_ENC	19	11	0	0	8	5,987	2	8	40,401,187
CONTRAGAN	35	14	13	1	7	4,131	9	3	9,416,196
CONTROLNET	427	121	132	0	174	N/A	56	7	39,726,979
COUNCIL_GAN	62	30	3	0	29	6,214	2	10	69,616,944
CLIPDM	226	120	34	0	72	N/A	38	3	113,673,219
CRAMER_GAN	9	4	1	0	4	454	2	3	9,681,284
CRGAN_C	35	14	13	1	7	4,131	9	3	9,416,196
CRGAN_P	35	14	13	1	7	4,131	9	3	9,416,196
CYCLEGAN	47	24	0	0	23	2,947	4	9	11,378,179
DAGAN_C	35	14	13	1	7	4,131	9	3	9,416,196
DAGAN_P	35	14	13	1	7	4,131	9	3	9,416,196
DCGAN	9	4	1	0	4	454	2	3	9,681,284
DDiFFGAN_32	289	80	91	0	118	N/A	40	2	48,432,515
DDPM_32	164	89	24	0	51	N/A	28	7	35,746,307
DDPM_256	225	120	34	0	71	N/A	39	7	113,673,219
DEEPOOL	95	92	1	2	0	7,236	4	10	22,000,000
DFCVAE	45	22	2	0	21	4,227	4	7	2,546,234
DIFF_ISGEN	88	24	56	0	8	N/A	8	6	30,276,583
DIFF_PGAN	45	20	0	3	13	N/A	11	4	105,684,175
DIFF_SGAN	48	20	28	0	8	N/A	8	6	24,767,458
DIFFAE	712	263	171	45	233	N/A	118	7	336,984,582
DIFFAE_LATENT	717	264	172	46	235	N/A	155	6	445,203,974
DISCOGAN	21	12	0	0	9	3,459	2	9	29,241,731
DRGAN	44	28	1	1	14	4,481	3	8	18,885,068
DRIT	19	10	0	0	9	1,793	4	3	9,564,170
DUALGAN	25	14	1	0	10	4,483	2	10	23,680,256
EBGAN	6	3	1	0	2	195	2	2	738,433
ESRGAN	66	66	0	0	0	4,547	5	4	7,012,163
FACTOR_VAE	7	4	3	0	0	99	1	3	469,173
Fast_pixel	17	9	0	0	8	768	2	8	4,600,000
FFGAN	39	19	1	1	19	3,261	0	0	50,000,000
FGAN	5	0	3	0	2	0	2	2	2,256,401
FGAN_KL	5	0	3	0	2	0	2	2	2,256,401
FGAN_NEYMAN	5	0	3	0	2	0	2	2	2,256,401
FGAN_PEARSON	5	0	3	0	2	0	2	2	2,256,401
FGSM	95	92	1	2	0	7,236	4	10	22,000,000
FPGAN	23	12	0	0	11	2,179	2	6	53,192,576
FSGAN	37	20	0	1	16	2,863	4	8	94,669,184
FVBN	28	0	28	0	0	0	1	1	307,721
GAN_ANIME	25	18	0	0	7	2,179	4	6	8,467,854
Gated_pixel_cnn	32	32	0	0	0	5,433	3	10	3,364,161
GDWCT	79	27	40	1	11	5,699	2	4	51,965,832
GFLM	95	92	1	2	0	7,236	4	10	22,000,000
GGAN	8	4	1	0	3	451	3	2	3,812,355
GLIDE	331	93	103	6	129	N/A	74	5	385,030,726
ICRGAN_C	35	14	13	1	7	4,131	9	3	9,416,196
ICRGAN_P	35	14	13	1	7	4,131	9	3	9,416,196

Table 14: Ground truth feature vector used for prediction of Continuous Architecture Hyperparameters for all GMs. The discrete architecture hyperparameter ground truth is defined in (Tab. 3). F1: # layers, F2: # convolutional layers, F3: # fully connected layers, F4: # pooling layers, F5: # normalization layers, F6: #filters, F7: # blocks, F8:# layers per block, and F9: # parameters.

GM	Layer #	Conv. #	FC #	Pool #	Norm. #	Filter #	Block #	Block Layer #	Para. #
IDDPM_32	193	85	32	0	76	N/A	45	2	52,546,438
IDDPM_64	195	87	32	0	76	N/A	45	2	27,3049,350
IDDPM_256	201	96	34	0	71	N/A	40	5	113,676,678
ILVER_256	266	107	45	11	103	N/A	39	7	553,838,086
Image_GPT	59	42	0	0	17	4,673	7	8	401,489
INFOGAN	7	3	1	0	3	195	2	2	1,049,985
LAPGAN	11	6	5	0	0	262	4	2	2,182,857
LDM	255	127	24	0	104	N/A	65	4	329,378,945
LDM_CON	503	159	184	8	152	N/A	65	8	456,755,873
Lmconv	105	60	10	35	0	7,156	15	5	46,000,000
LOGAN	35	14	13	1	7	4,131	9	3	9,416,196
LSGAN	9	5	0	0	4	1,923	2	4	23,909,265
MADE	2	0	2	0	0	0	1	2	12552784
MAGAN	9	5	0	0	4	963	2	3	11,140,934
MEMGAN	14	7	1	0	6	1,155	3	4	4,128,515
MMD_GAN	9	4	1	0	4	454	2	3	9,681,284
MRGAN	9	4	1	0	4	451	3	2	15,038,350
MSG_STYLE_GAN	33	25	8	0	0	4,094	3	8	50,200,000
MUNIT	18	15	0	0	3	3,715	2	6	10,305,035
NADE	1	0	1	0	0	0	1	1	785,284
OCFGAN	9	4	1	0	4	454	2	3	9,681,284
PGD	95	92	1	2	0	7,236	4	10	22,000,000
PIX2PIX	29	16	0	0	13	5,507	2	13	54,404,099
PixelCNN	17	9	0	0	8	768	2	8	4,600,000
PixelCNN++	105	60	10	35	0	7,156	15	5	46,000,000
PIXELDA	27	14	1	0	12	835	4	6	483,715
PixelSnail	90	90	0	0	0	4,051	3	10	40,000,000
PNDM_32	164	89	24	0	51	N/A	28	7	35,746,307
PNDM_256	266	107	45	11	103	N/A	39	7	553,838,086
PROG_GAN	26	25	1	0	0	4,600	3	8	46,200,000
RGAN	7	3	1	0	3	195	2	2	1,049,985
RSGAN_HALF	8	4	1	0	3	899	3	2	13,129,731
RSGAN_QUAR	8	4	1	0	3	451	3	2	3,812,355
RSGAN_REG	8	4	1	0	3	1,795	3	2	48,279,555
RSGAN_RES_BOT	15	7	1	0	7	963	3	4	758,467
RSGAN_RES_HALF	15	7	1	0	7	1,155	3	4	1,201,411
RSGAN_RES_QUAR	15	7	1	0	7	579	3	4	367,235
RSGAN_RES_REG	15	7	1	0	7	2,307	3	4	4,270,595
SAGAN	11	6	1	0	4	139	2	4	16,665,286
SEAN	19	16	0	0	0	5,062	2	7	266,907,367
SEMANTIC	23	12	0	0	11	2,179	2	6	53,192,576
SGAN	7	3	1	0	3	195	2	2	1,049,985
SCOREDIFF_256_225	120	34	0	11	71	N/A	39	7	113,673,219
SDeDif	226	120	34	0	72	N/A	38	3	113,673,219
SNGAN	23	11	1	0	11	3,871	4	5	10,000,000
SOFT_GAN	8	0	5	0	3	0	2	3	1,757,412
SRRNET	66	66	0	0	2	4,547	5	4	7,012,163
SRFLOW	74	36	1	0	37	2,819	4	16	4,069,955
STANDARD_VAE	7	4	3	0	0	99	1	3	469,173
STARGAN	23	12	0	0	11	2,179	2	6	53,192,576
STARGAN_2	67	26	12	4	25	4,188	4	12	94,008,488
STA_DM_15	503	159	184	8	152	N/A	65	8	456,755,873
STA_DM_21	503	159	184	8	152	N/A	65	8	456,755,873
STA_DM_XL	601	184	201	12	185	N/A	74	9	618,997,638
STGAN	19	10	0	0	9	2,953	2	5	25,000,000
STYLEGAN	33	25	8	0	0	4,094	3	8	50,200,000
STYLEGAN_2	33	25	8	0	0	4,094	3	8	59,000,000
STYLEGAN2_ADA	33	25	8	0	0	4,094	3	8	59,000,000
SURVAE_FLOW_MAX	95	90	0	5	0	6,542	2	20	25,000,000
SURVAE_FLOW_NON	90	90	0	0	0	6,542	2	20	25,000,000
TPGAN	45	31	2	1	11	5,275	0	0	27,233,200
UGAN	9	4	1	0	4	771	2	3	4,850,692
UNIT	43	22	0	0	21	4,739	4	8	13,131,779
VAE_field	6	0	6	0	0	0	1	3	300,304
VAE_flow	14	0	14	0	0	0	2	4	760,448
VAEGAN	17	7	2	0	8	867	2	6	26,396,740
VDVAE	48	42	0	6	0	3,502	3	13	41,000,000
WGAN	9	5	0	0	4	1,923	2	4	23,909,265
WGAN_DRA	18	10	1	0	7	2,307	5	3	4,276,739
WGAN_WC	18	10	1	0	7	2,307	5	3	4,276,739
WGANP	9	5	0	0	4	1,923	2	4	23,905,841
YLG	33	20	1	2	10	5,155	5	5	42,078,852

References

1. AbdAlmageed, W., Mirzaalian, H., Guo, X., Randolph, L.M., Tanawat-tanacharoen, V.K., Geffner, M.E., Ross, H.M., Kim, M.S.: Assessment of facial morphologic features in patients with congenital adrenal hyperplasia using deep learning. *JAMA network open* (2020) [14](#)
2. Asnani, V., Yin, X., Hassner, T., Liu, X.: Malp: Manipulation localization using a proactive scheme. In: *CVPR* (2023) [1](#)
3. Asnani, V., Yin, X., Hassner, T., Liu, X.: Reverse engineering of generative models: Inferring model hyperparameters from generated images. *IEEE Transactions on Pattern Analysis and Machine Intelligence* (2023) [1](#), [2](#), [3](#), [4](#), [5](#), [10](#), [14](#)
4. Batina, L., Bhasin, S., Jap, D., Picek, S.: CSI NN: Reverse engineering of neural network architectures through electromagnetic side channel. In: *USENIXSS* (2019) [4](#)
5. Chai, L., Bau, D., Lim, S.N., Isola, P.: What makes fake images detectable? understanding properties that generalize. In: *European Conference on Computer Vision* (2020) [2](#), [4](#), [13](#), [10](#)
6. Chen, D., Lin, Y., Li, W., Li, P., Zhou, J., Sun, X.: Measuring and relieving the over-smoothing problem for graph neural networks from the topological view. In: *Proceedings of the AAAI conference on artificial intelligence*. vol. 34, pp. 3438–3445 (2020) [8](#)
7. Chen, L., Zhang, Y., Song, Y., Liu, L., Wang, J.: Self-supervised learning of adversarial example: Towards good generalizations for deepfake detection. In: *CVPR* (2022) [1](#)
8. Chen, T., Xu, M., Hui, X., Wu, H., Lin, L.: Learning semantic-specific graph representation for multi-label image recognition. In: *Proceedings of the IEEE/CVF international conference on computer vision*. pp. 522–531 (2019) [2](#), [4](#)
9. Chen, Y., Xia, S., Zhao, J., Zhou, Y., Niu, Q., Yao, R., Zhu, D., Liu, D.: Rest-reid: Transformer block-based residual learning for person re-identification. *Pattern Recognition Letters* **157**, 90–96 (2022) [4](#)
10. Chen, Y., Rohrbach, M., Yan, Z., Shuicheng, Y., Feng, J., Kalantidis, Y.: Graph-based global reasoning networks. In: *Proceedings of the IEEE/CVF conference on computer vision and pattern recognition*. pp. 433–442 (2019) [4](#)
11. Chen, Z.M., Wei, X.S., Wang, P., Guo, Y.: Multi-label image recognition with graph convolutional networks. In: *Proceedings of the IEEE/CVF conference on computer vision and pattern recognition*. pp. 5177–5186 (2019) [2](#), [4](#)
12. Choi, Y., Choi, M., Kim, M., Ha, J.W., Kim, S., Choo, J.: StarGAN: Unified generative adversarial networks for multi-domain image-to-image translation. In: *CVPR* (2018) [1](#)
13. Corvi, R., Cozzolino, D., Zingarini, G., Poggi, G., Nagano, K., Verdoliva, L.: On the detection of synthetic images generated by diffusion models. In: *ICASSP 2023-2023 IEEE International Conference on Acoustics, Speech and Signal Processing (ICASSP)*. pp. 1–5. IEEE (2023) [4](#)
14. Deng, J., Dong, W., Socher, R., Li, L.J., Li, K., Fei-Fei, L.: Imagenet: A large-scale hierarchical image database. In: *2009 IEEE conference on computer vision and pattern recognition*. pp. 248–255. Ieee (2009) [7](#)
15. Dhariwal, P., Nichol, A.: Diffusion models beat gans on image synthesis. *Advances in Neural Information Processing Systems* **34**, 8780–8794 (2021) [5](#)
16. Ding, H., Zhang, H., Liu, J., Li, J., Feng, Z., Jiang, X.: Interaction via bi-directional graph of semantic region affinity for scene parsing. In: *Proceedings*

- of the IEEE/CVF International Conference on Computer Vision. pp. 15848–15858 (2021) [2](#), [4](#)
17. Fan, W., Ma, Y., Li, Q., He, Y., Zhao, E., Tang, J., Yin, D.: Graph neural networks for social recommendation. In: The world wide web conference. pp. 417–426 (2019) [2](#), [4](#)
 18. Gao, H., Ji, S.: Graph u-nets. In: international conference on machine learning. pp. 2083–2092. PMLR (2019) [4](#), [11](#)
 19. Gerstner, C.R., Farid, H.: Detecting real-time deep-fake videos using active illumination. In: CVPR (2022) [1](#)
 20. Goodfellow, I., Pouget-Abadie, J., Mirza, M., Xu, B., Warde-Farley, D., Ozair, S., Courville, A., Bengio, Y.: Generative adversarial nets. In: NeurIPS (2014) [1](#)
 21. Guo, X., Choi, J.: Human motion prediction via learning local structure representations and temporal dependencies. In: AAAI (2019) [14](#)
 22. Guo, X., Liu, X., Ren, Z., Grosz, S., Masi, I., Liu, X.: Hierarchical fine-grained image forgery detection and localization. In: In Proceeding of IEEE Computer Vision and Pattern Recognition (2023) [1](#), [4](#), [10](#), [14](#)
 23. Guo, X., Liu, Y., Jain, A., Liu, X.: Multi-domain learning for updating face anti-spoofing models. In: ECCV (2022) [7](#)
 24. Guo, X., Mirzaalian, H., Sabir, E., Jaiswal, A., Abd-Almageed, W.: Cord19sts: Covid-19 semantic textual similarity dataset. arXiv preprint arXiv:2007.02461 (2020) [14](#)
 25. Guo, Z., Zhang, Y., Lu, W.: Attention guided graph convolutional networks for relation extraction. In: Proceedings of the 57th Annual Meeting of the Association for Computational Linguistics. pp. 241–251 (2019) [4](#)
 26. Ho, J., Jain, A., Abbeel, P.: Denoising diffusion probabilistic models. *Advances in Neural Information Processing Systems* **33**, 6840–6851 (2020) [5](#)
 27. Hsu, I., Guo, X., Natarajan, P., Peng, N.: Discourse-level relation extraction via graph pooling. In: AAAI DLG workshop (2021) [4](#)
 28. Hu, H., Ji, D., Gan, W., Bai, S., Wu, W., Yan, J.: Class-wise dynamic graph convolution for semantic segmentation. In: European Conference on Computer Vision. pp. 1–17. Springer (2020) [4](#)
 29. Hua, W., Zhang, Z., Suh, G.E.: Reverse engineering convolutional neural networks through side-channel information leaks. In: DAC (2018) [4](#)
 30. Ji, K., Chen, F., Guo, X., Xu, Y., Wang, J., Chen, J.: Uncertainty-guided learning for improving image manipulation detection. In: Proceedings of the IEEE/CVF International Conference on Computer Vision. pp. 22456–22465 (2023) [1](#)
 31. Karras, T., Aila, T., Laine, S., Lehtinen, J.: Progressive growing of gans for improved quality, stability, and variation. In: Int. Conf. Learn. Represent. (2018) [1](#), [12](#), [7](#)
 32. Karras, T., Laine, S., Aila, T.: A style-based generator architecture for generative adversarial networks. In: CVPR. pp. 4401–4410 (2019) [1](#), [7](#)
 33. Kim, G., Kwon, T., Ye, J.C.: DiffusionCLIP: Text-guided diffusion models for robust image manipulation. In: CVPR (2022) [1](#)
 34. Kipf, T.N., Welling, M.: Semi-supervised classification with graph convolutional networks. arXiv preprint arXiv:1609.02907 (2016) [2](#), [4](#)
 35. Krizhevsky, A., Hinton, G., et al.: Learning multiple layers of features from tiny images. Tech. rep., Citeseer (2009) [7](#)
 36. LeCun, Y., Bottou, L., Bengio, Y., Haffner, P.: Gradient-based learning applied to document recognition. *Proceedings of the IEEE* **86**(11), 2278–2324 (1998) [7](#)

37. Li, G., Muller, M., Thabet, A., Ghanem, B.: Deepgcns: Can gcns go as deep as cnns? In: Proceedings of the IEEE/CVF international conference on computer vision. pp. 9267–9276 (2019) [8](#)
38. Li, X., Yang, Y., Zhao, Q., Shen, T., Lin, Z., Liu, H.: Spatial pyramid based graph reasoning for semantic segmentation. In: Proceedings of the IEEE/CVF Conference on Computer Vision and Pattern Recognition. pp. 8950–8959 (2020) [4](#)
39. Li, Y., Yang, X., Sun, P., Qi, H., Lyu, S.: Celeb-df: A new dataset for deepfake forensics. arXiv preprint arXiv:1909.12962 (2019) [13](#)
40. Li, Y., Yang, X., Sun, P., Qi, H., Lyu, S.: Celeb-df: A large-scale challenging dataset for deepfake forensics. In: Proceedings of the IEEE/CVF conference on computer vision and pattern recognition. pp. 3207–3216 (2020) [13](#), [10](#)
41. Marra, F., Gragnaniello, D., Verdoliva, L., Poggi, G.: Do gans leave artificial fingerprints? In: IEEE conference on multimedia information processing and retrieval (MIPR) (2019) [4](#), [14](#)
42. Medin, S.C., Egger, B., Cherian, A., Wang, Y., Tenenbaum, J.B., Liu, X., Marks, T.K.: MOST-GAN: 3D morphable StyleGAN for disentangled face image manipulation. In: AAAI (2022) [1](#)
43. Min, Y., Wenkel, F., Wolf, G.: Scattering gcn: Overcoming oversmoothness in graph convolutional networks. Advances in neural information processing systems **33**, 14498–14508 (2020) [8](#)
44. Nataraj, L., Mohammed, T.M., Manjunath, B., Chandrasekaran, S., Flenner, A., Bappy, J.H., Roy-Chowdhury, A.K.: Detecting gan generated fake images using co-occurrence matrices. Electronic Imaging **31**, 1–7 (2019) [13](#), [10](#)
45. Nguyen, B.X., Nguyen, B.D., Do, T., Tjiputra, E., Tran, Q.D., Nguyen, A.: Graph-based person signature for person re-identifications. In: Proceedings of the IEEE/CVF conference on computer vision and pattern recognition. pp. 3492–3501 (2021) [2](#), [4](#)
46. Oh, S.J., Augustin, M., Fritz, M., Schiele, B.: Towards reverse-engineering black-box neural networks. In: ICLR (2018) [4](#)
47. Ojha, U., Li, Y., Lee, Y.J.: Towards universal fake image detectors that generalize across generative models. In: Proceedings of the IEEE/CVF Conference on Computer Vision and Pattern Recognition. pp. 24480–24489 (2023) [4](#), [7](#), [12](#), [13](#), [10](#)
48. Rombach, R., Blattmann, A., Lorenz, D., Esser, P., Ommer, B.: High-resolution image synthesis with latent diffusion models (2021) [5](#)
49. Schlichtkrull, M., Kipf, T.N., Bloem, P., Van Den Berg, R., Titov, I., Welling, M.: Modeling relational data with graph convolutional networks. In: The Semantic Web: 15th International Conference, ESWC 2018, Heraklion, Crete, Greece, June 3–7, 2018, Proceedings 15. pp. 593–607. Springer (2018) [2](#)
50. Sencar, H.T., Verdoliva, L., Memon, N.: Multimedia Forensics. Springer Nature (2022) [1](#)
51. Shiohara, K., Yamasaki, T.: Detecting deepfakes with self-blended images. In: CVPR (2022) [1](#)
52. Sun, Z., Jiang, H., Wang, D., Li, X., Cao, J.: Saff-net: Semantic-agnostic feature learning network with auxiliary plugins for image manipulation detection. In: Proceedings of the IEEE/CVF International Conference on Computer Vision. pp. 22424–22433 (2023) [1](#)
53. Tirupattur, P., Duarte, K., Rawat, Y.S., Shah, M.: Modeling multi-label action dependencies for temporal action localization. In: Proceedings of the IEEE/CVF Conference on Computer Vision and Pattern Recognition. pp. 1460–1470 (2021) [2](#), [4](#)

54. Tramèr, F., Zhang, F., Juels, A., Reiter, M.K., Ristenpart, T.: Stealing machine learning models via prediction APIs. In: USENIXSS (2016) [4](#)
55. Tran, L., Yin, X., Liu, X.: Disentangled representation learning GAN for pose-invariant face recognition. In: CVPR (2017) [1](#)
56. Veličković, P., Cucurull, G., Casanova, A., Romero, A., Lio, P., Bengio, Y.: Graph attention networks. arXiv preprint arXiv:1710.10903 (2017) [2](#), [4](#), [11](#)
57. Wang, S.Y., Wang, O., Zhang, R., Owens, A., Efros, A.A.: Cnn-generated images are surprisingly easy to spot... for now. In: IEEE Conf. Comput. Vis. Pattern Recog. pp. 8695–8704 (2020) [1](#), [2](#), [4](#), [7](#), [10](#), [12](#), [13](#)
58. Wang, Z., Bao, J., Zhou, W., Wang, W., Hu, H., Chen, H., Li, H.: Dire for diffusion-generated image detection. arXiv preprint arXiv:2303.09295 (2023) [2](#), [4](#), [13](#), [10](#)
59. Wu, Y., AbdAlmageed, W., Natarajan, P.: Mantra-net: Manipulation tracing network for detection and localization of image forgeries with anomalous features. In: IEEE Conf. Comput. Vis. Pattern Recog. pp. 9543–9552 (2019) [1](#)
60. Yao, Y., Jiang, X., Fujita, H., Fang, Z.: A sparse graph wavelet convolution neural network for video-based person re-identification. Pattern Recognition **129**, 108708 (2022) [4](#)
61. Yao, Y., Guo, X., Asnani, V., Gong, Y., Liu, J., Lin, X., Liu, X., Liu, S., et al.: Reverse engineering of deceptions on machine-and human-centric attacks. Foundations and Trends® in Privacy and Security **6**(2), 53–152 (2024) [4](#)
62. Ye, J., He, J., Peng, X., Wu, W., Qiao, Y.: Attention-driven dynamic graph convolutional network for multi-label image recognition. In: Computer Vision–ECCV 2020: 16th European Conference, Glasgow, UK, August 23–28, 2020, Proceedings, Part XXI 16. pp. 649–665. Springer (2020) [2](#), [4](#)
63. Yu, F., Seff, A., Zhang, Y., Song, S., Funkhouser, T., Xiao, J.: Lsun: Construction of a large-scale image dataset using deep learning with humans in the loop. arXiv preprint arXiv:1506.03365 (2015) [7](#)
64. Yu, N., Davis, L.S., Fritz, M.: Attributing fake images to GANs: Learning and analyzing GAN fingerprints. In: ICCV. pp. 7556–7566 (2019) [4](#), [10](#)
65. Yu, N., Davis, L.S., Fritz, M.: Attributing fake images to gans: Learning and analyzing gan fingerprints. In: Proceedings of the IEEE/CVF international conference on computer vision. pp. 7556–7566 (2019) [14](#)
66. Zhai, Y., Luan, T., Doermann, D., Yuan, J.: Towards generic image manipulation detection with weakly-supervised self-consistency learning. In: Proceedings of the IEEE/CVF International Conference on Computer Vision. pp. 22390–22400 (2023) [1](#)
67. Zhang, X., Karaman, S., Chang, S.F.: Detecting and simulating artifacts in gan fake images. In: 2019 IEEE international workshop on information forensics and security (WIFS). pp. 1–6. IEEE (2019) [2](#), [4](#)
68. Zhang, X., Karaman, S., Chang, S.F.: Detecting and simulating artifacts in gan fake images. In: WIFS (2019) [12](#), [13](#), [10](#)
69. Zhou, J., Ma, X., Du, X., Alhamadi, A.Y., Feng, W.: Pre-training-free image manipulation localization through non-mutually exclusive contrastive learning. In: Proceedings of the IEEE/CVF International Conference on Computer Vision. pp. 22346–22356 (2023) [1](#)